COMPUTATIONAL CHEMISTRY AS A TOOL FOR UNDERSTANDING NON-COVALENT INTERACTIONS IN ORGANIC REACTIONS AND MATERIALS

A Dissertation

by

DIANA SEPULVEDA CAMARENA

Submitted to the Office of Graduate and Professional Studies of
Texas A&M University
in partial fulfillment of the requirements for the degree of

DOCTOR OF PHILOSOPHY

Chair of Committee,	Steven E. Wheeler
Committee Members,	Daniel Romo
	David E. Bergbreiter
	Robert C. Alaniz
Head of Department,	David H. Russsell

December 2014

Major Subject: Chemistry

ABSTRACT

Non-covalent interactions (NCIs) play vital roles in many areas of chemistry and materials science. Although there has been a great deal of progress understanding the nature of non-covalent interactions in recent years, many aspects of these phenomena are still unclear. Modern DFT methods have become a valuable tool for organic chemists in studies of systems in which dispersion-driven NCIs are vital. The role of non-covalent interactions in two organocatalyzed reactions and two novel organic materials were studied by means of these and other computational tools.

The two organocatalyzed reactions presented are the allylation and propargylation reactions catalyzed by a bipyridine *N,N*'-dioxide catalyst and a hetero-Diels – Alder reaction catalyzed by a cage-shaped borate catalyst. In the first case, the reaction was used as an example to benchmark DFT methods against high accuracy *ab initio* calculations. It was shown that B97-D/TZV*(2d,2p)* provides the best compromise of accuracy and computational efficiency. Additionally, it was demonstrated that the original transition state model used to explain the stereoselectivity of these reactions is flawed. We developed a simple model based on non-covalent electrostatic interactions that explains the stereoselectivity of these reactions as well as the fact that the propargylation reaction is less stereoselective than the allylation. For the second reaction, preliminary results provide some support that π-stacking interactions between the substrate and the catalyst are responsible for the selective reaction of aromatic over aliphatic aldehydes, as observed experimentally.

In an effort to better control the properties of organic materials based on discotic systems, stacking interactions between contorted hexabenzocoronene (*c*-HBC) homodimers

and complexes of *c*-HBC with C_{60} fullerene were studied using DFT methods. It was found that the preference to stack as homo or heterodimers can be tuned by controlling the curvature of the *c*-HBC. To achieve this, different substituents on the *c*-HBC were tested. However, only perfluorination imparts sufficient curvature to the c-HBC to lead to tip the balance towards heterodimer formation over homodimer formation. Finally, an additional explanation was provided for the rotational speed difference between the –OH and –OMe substituted pillar[5]arenes. It is shown that in addition to the hydrogen bond explanation for the –OH substituted case provided by Ogishi and coworkers (*J. Phys.Chem. Lett*.**,2010**, 817), non-covalent CH/π interactions contribute significantly to the TS stabilization of the –OMe substituted case, enhancing the rotational speed.

DEDICATION

A mi familia: Marilú, David, Ale, Chucho y Ana

Les dedico estos seis años de trabajo y aprendizaje.

¡Los amo!

Diana

ACKNOWLEDGEMENTS

I would like to thank my committee chair, Dr. Wheeler, for giving me the opportunity to join his research group; it was an enriching and enjoyable experience working with you. I also want to thank my committee members, Dr. Bergbreiter for his valuable teaching lessons, Dr. Romo for giving me the opportunity to do research in his laboratory as an undergraduate – if it had not been for him I would have probably not pursued a graduate degree, and Dr. Alaniz for his guidance and support throughout the course of this research. Additionally, thanks to the financial support from the Welch Foundation (Grant A-1775) and the National Science Foundation (Grant CHE-1266022).

Thanks to Sandy Manning for always helping me navigate the school's procedures and meet the necessary requirements for the Ph.D. program on time. Thanks to Carrie Nichols and Janet Robinson for being so patient at the beginning of my teaching assistantship, I really appreciate them being cheerful as well as always having a sweet treat right when I needed it the most. I am grateful to all the Wheeler group members for always being willing to help - with anything from scripting, to attending the practices for my interviews.

Personally, I would like to thank my friend Dr. Maria Duran Galvan; she was a role model of hard work and persistence through my early graduate school journey as well as my unconditional friend. Thank you to Francisco Escobedo, my roommate, for offering his unconditional help whether it was chemistry related or moving – apartments related. Both of you made my tough times through graduate school feel lighter. I want to give special thanks to Ashley Gould, her courage and advice was a motivation to not give up and be confident in myself.

Finally, thanks to my mother and father for their encouragement and support and for teaching me to work hard to pursue my dreams. Thanks to my aunt Ana, for listening to me, for her encouragement and financial support whenever needed. Thank you to my brother and sister, for believing in me, for making me laugh, for reminding me that tough times can only last so long and that one cannot take them so seriously. Last, but not least, thank you to my now husband, Christopher E. Hobbs, for supporting unconditionally every career decision I have made so far, even when at times those decisions have kept us away from each other. To all of you in my family: thanks and I love you!

TABLE OF CONTENTS

Page

LIST OF FIGURES

Page

LIST OF TABLES

Page

1. INTRODUCTION

Non-covalent interactions play vital roles in many areas of chemistry and materials science. Although there has been a great deal of progress understanding the nature of non-covalent interactions in recent years, many aspects of these phenomena are still unclear. Moreover, there are still significant gaps in our understanding of the quantitative role these non-covalent interactions play in many areas of organic chemistry. Ultimately, we will need to deepen our understanding of non-covalent interactions in order to fully exploit their power in chemical applications. Here, we strive to understand the role of non-covalent interactions in the areas of organocatalyzed reactions and organic materials.

1.1 Non-Covalent Interactions (NCIs)

Atoms can interact with one another in two basic manners: covalently and non-covalently. A covalent interaction involves the sharing of electrons and results in a covalent bond, which is traditionally considered the backbone of complex molecules. On the other hand, non-covalent interactions (NCIs) can be defined as a type of chemical bond that does not involve the sharing of electron pairs, but instead involves more dispersed variations of electromagnetic interactions. These kinds of interactions are weaker and simpler than covalent bonds, and, because they produce large binding forces when added up together, are often cooperative. While covalent interactions give rise to molecules, NCIs give rise to molecular clusters and the supramolecular assemblies that are at the heart of many areas of modern chemical research.

J.D. van der Waals was the first to recognize non-covalent interactions, when in the 1870s, he suggested that significant attractive forces exist between gas molecules. An

important landmark in the history of understanding these attractive forces was provided by the liquefaction of helium by Kamerlingh-Onnes. Later, in 1930, Fritz London was the first to provide a theoretical treatment of the attractive interactions between non polar molecules and atoms. This interaction, which he attributed to instantaneous fluctuations in the charge distributions in molecules, is now known as the dispersion force (or London dispersion force).

Since then, interest from the scientific community on these interactions has grown. Particularly, there has been an explosive increase in the number of publications on non-covalent interactions over the last 25 years. This rapid rise in the number of publications can be associated with the ready availability of computational methods to treat these interactions, as discussed below. Historically, NCIs have been classified in a variety of ways, mainly depending on the context. In the broadest sense, NCIs can be classified based on the distribution of charge within the interacting bodies and how the strength of the interaction varies with the distance between interacting species (r). Basic types of NCIs classified this way are listed in Table 1[1]

Table 1 Classification of Non-Covalent Interactions

	Strength [kJ/mol]	**Energy dependence on distance**	**Examples**
Charge-Charge		$1/r$	Ion pairs
Charge – Dipole	50-200 kJ/mol	$1/r^2$	Na^+ - H_2O
Dipole – Dipole	5-50 kJ/mol	$1/r^3$	HCl – HCl
Charge – Induced Dipole	5-80 kJ /mol	$1/r^4$	Na^+ - Ar
Dipole – Induced Dipole	~ 5 kJ/mol	$1/r^5$	HCl – Ar
Dispersion	< 5 kJ/mol	$1/r^6$	Non-ideal behavior of gases, π-π
H- bond	4 – 120 kJ/mol	$\approx 1/r^2$	Water H-bond

More qualitatively, chemists typically define a number of prototypical NCIs, some of which are depicted in Figure 1. Chief among these are hydrogen bonding interactions, which underlie many chemical and, particularly, biochemical phenomena. However, there has been growing interest in recent years in the many non-covalent interactions involving aromatic rings, including π-stacking interactions, XH/π interactions, cation-π interactions, and anion-π interactions, among others. Together, these interactions, often mischaracterized as "aromatic interactions,"[2] can exert enormous influence over many different chemical phenomena. Many aspects of these interactions have only recently been uncovered.

Figure 1 Prototypical NCIs of importance in chemistry.

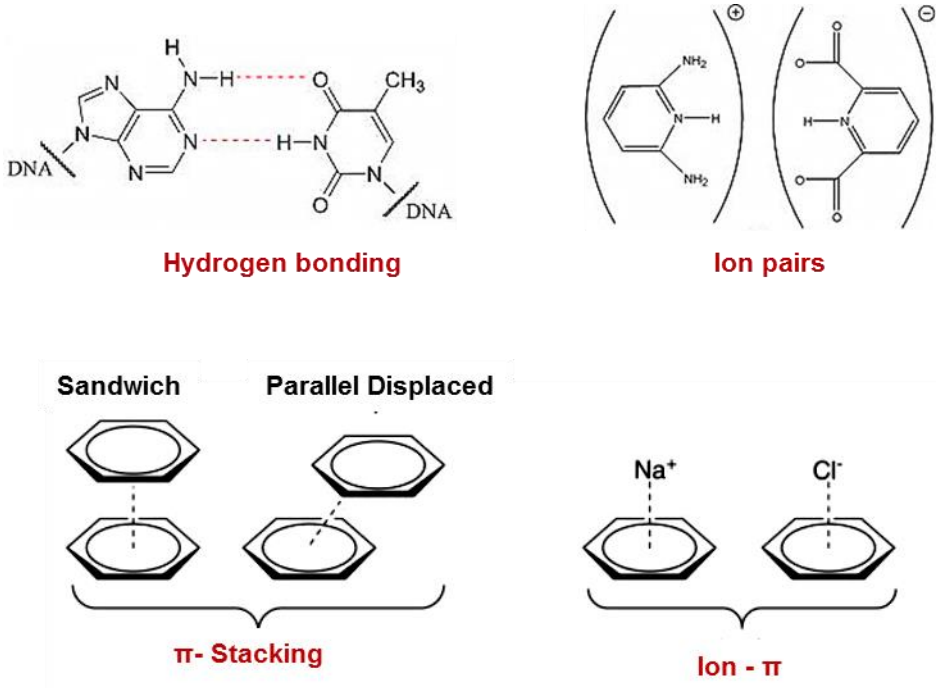

1.2 Theoretical Description of NCIs

NCIs can be studied by standard methods of quantum chemistry based either on perturbation theory or variational methods. Perturbation methods separate the overall interaction energy into various physically well-defined contributions such as electrostatic, induction, dispersion and exchange-repulsion energies, while variational methods separate the interaction only into Hartree-Fock and posts HF (correlation) contributions. Importantly, neither the Hartree-Fock energy or correlation energy are directly observable. Of course, neither are the individual energy contributions in the perturbation theory expansion.

Dispersion effects play a central role in many non-covalent complexes. However, because dispersion effects are due to the correlation of electron motion, their computational description requires correlated *ab initio* methods paired with large basis sets. This requirement can become computationally expensive and time consuming. Therefore, finding more practical, less-time consuming yet accurate approaches for these interactions is an active area of research for computational chemists. To target this issue, in recent years, DFT and LPNO methods have been successfully applied to the study of NCIs. However, the careful selection of computational method is highly dependent on the targeted system of study. At the same time, with the increasing number of available DFT methods, selecting a level of theory that agrees with experimental observations and, most importantly, delivers reliable results, can become a daunting task for chemists.

To study organic systems, which can include 100+ atoms, DFT methods are the natural choice given their relatively low computational cost. There have been many advances the last few years in DFT methods that can treat NCIs in general, and dispersion interactions in particular. As a result, there have been a significant number of recent

examples of previously proposed organic models that have been re-evaluated by taking NCIs into account. This has resulted in many unexpected results that ultimately lead to a better understanding of reaction mechanisms, *etc*. With the increasing availability of computational resources as well as more user-friendly programs, it is becoming increasingly common for organic chemists to do the necessary calculations themselves. Above all, physical organic chemists have to be able to choose an appropriate level of theory for the desired system of study, finding a compromise between accuracy and computational cost. In the following sections, we will present a brief description of the methods that were used to carry out the present work. Technical details about the methods employed can be found in the methods sections of the following chapters.

1.2.1 *Ab initio* Methods

The term *ab initio* refers to the fact that these methods rely exclusively in physical constants and the Schrödinger equation, not experimental data. There are other levels of theory (semi-empirical methods) that, in contrast, make use of experimental data in the form of adjustable parameters. For a molecule, the time-independent Schrödinger equation is given by:

$$\hat{H}\psi = E\psi \tag{1}$$

where ψ is a many-electron wavefunction and $\hat{H}$ is the Hamiltonian, which, in atomic units, is given by:

$$\hat{H} = -\frac{1}{2}\sum_{i}^{electrons}\nabla_i^2 - \frac{1}{2}\sum_{A}^{nuclei}\frac{1}{M_A}\nabla_A^2 - \sum_{i}^{electrons}\sum_{A}^{nuclei}\frac{Z_A}{r_{iA}} + \sum_{i}^{electrons}\sum_{j>i}^{electrons}\frac{1}{r_{ij}} + \sum_{A}^{nuclei}\sum_{B>A}^{nuclei}\frac{Z_A Z_B}{R_{AB}} \tag{2}$$

where Z_A and M_A are the nuclear charge and mass of atom A, R_{AB} is the distance between nuclei A and B, r_{ij} is the distance between electrons *i* and *j*, and r_{iA} is the distance between electron *i* and nucleus A.

Since the many-electron Schrödinger equation cannot be solved exactly, approximations are required to provide practical results. More specifically, most *ab initio* calculations are based on the Born–Oppenheimer (BO) approximation, which greatly simplifies the Schrödinger equation by freezing the nuclei in place during the calculation. By doing so, an "electronic" version of the Schrödinger equation is obtained:

$$\hat{H}^{el}\psi^{el} = E^{el}\psi^{el} \tag{3}$$

After removing the nuclear kinetic energy term from equation 2, and making the nuclear – nuclear Coulomb term a constant, the Hamiltonian is given by:

$$\hat{H}^{el} = -\frac{1}{2}\sum_{i}^{electrons}\nabla_i^2 - \sum_{i}^{electrons}\sum_{A}^{nuclei}\frac{Z_A}{r_{iA}} + \sum_{i}^{electrons}\sum_{j>i}^{electrons}\frac{1}{r_{ij}} \tag{4}$$

The nuclear-nuclear Coulomb constant is then added to the electronic energy, E^{el}, to provide the total energy of the system, E:

$$E = E^{el} + \sum_{A}^{nuclei}\sum_{B>A}^{nuclei}\frac{Z_A Z_B}{R_{AB}} \tag{5}$$

The electronic Schrödinger equation is still unsolvable (except in the limiting case of one electron) and further approximations are needed. There are a variety of methods that can be used to approximately solve the electronic Schrödinger equation. In general, the accuracy of these methods increases as the approximations made are reduced. The main distinction between *ab initio* methods is the extent to which they treat electron correlation. Correlation effects arise from instantaneous interactions between electrons, and can be estimated by

adding effects of admixtures of excited states into the Hartree-Fock determinant. The later can be accomplished through perturbation methods such as Møller-Plesset (MP) or by including excited state determinants in the wave equation as in configuration interaction calculations. Below, we review common *ab initio* methods, focusing on those used in the present work.

1.2.1.1 Hartree-Fock (HF) Theory

Hartree-Fock theory was introduced by D.R. Hartree and V. Fock in the 1920s to calculate approximate wave functions and energies for atoms and ions. This method is the origin of molecular orbitals (MOs), which are the workhorse of traditional theoretical organic chemists. In HF theory, one assumes that the wavefunction takes the form of a single antisymmetrized product of occupied MOs (Slater determinant), and then finds the set of MOs that minimizes the quantum mechanical energy of this wavefunction. This set of MOs is obtained by a process referred to as the "self-consistent-field," or SCF procedure. The HF wavefunction and energy provides the first approximation to the ground state wavefunction and energy of the system, and serves as a base for further approximations, as explained below. HF theory does not capture instantaneous electron-electron interactions. Instead, it accounts for the interaction of each electron with the average distribution of the other electrons. As such, these methods are not used directly to study NCIs, since they are unable to capture the instantaneous electronic interactions that are at the root of dispersion interactions.

1.2.1.2 Second-order Møller–Plesset Theory (MP2)

Second order MP2 is the simplest model of the Møller–Plesset series (MP*n*), which provide means of improving HF theory by accounting for the effects of electron correlation effects via Rayleigh–Schrödinger perturbation theory. MP*n* methods are size consistent but not variational. MP2 is well-suited to study NCIs, being the simplest ab initio method to capture instantaneous interactions between pairs of electrons. However, MP2 tends to overestimate dispersion effects.

1.2.1.3 Coupled-Cluster (CC) theory

The term coupled-cluster was introduced by Coester and Kümmel to calculate binding energies in nuclei that could be treated in the first approximation by a single configuration of neutrons or protons. It was later adapted for the electronic structure problem by Cizek, Paldus, and Shavitt in the late 1960s and early 1970s.[3-5] It was not until the 1980s, when Purvis and Bartlett introduced a practical coupled cluster program,[6] that applications of coupled cluster theory to molecules became feasible. Coupled cluster theory builds on Hartree–Fock determinant by constructing multi-electron wave functions using an exponential cluster operator to account for electron correlation effects. The method is size consistent, unitarily invariant, and converges rapidly toward the exact solution to the electronic Schrodinger equation (full CI limit). Although the CCSD(T) method is considered a "gold standard" for high-level *ab initio* calculations, and provides excellent descriptions of NCIs, it is computationally expensive. Therefore, it is typically used to study small or medium size molecules (~10-20 atoms).

1.2.1.4 Coupled Electron Pair Approximation (CEPA)

Coupled electron pair approximation (CEPA) methods were developed in the 1970s and 1980s by Meyer, Kutzelnigg, Ahlrichs, Hurley and Taylor in order to reduce the high-order scaling of the CC methods with the size of the system. Although these methods fell out of favor in the years that followed, CEPA methods were recently resurrected by Neese and co-workers, who showed that the exploitation of the localized MOs could lead to highly-efficient and accurate CEPA methods applicable to large molecules (~100 atoms). These so-called LPNO methods are not linear scaling but they are highly accurate and efficient local correlation methods.[7-9] They are also more accurate than MP2 or DFT based approaches and, hence, can be applied as accurate model chemistries for large systems (20-100 atoms) in large saturated basis sets (up to 2500 basis functions). Among the various approximations available, LPNO-CEPA/1 has been shown to have a good performance to describe non-covalent interactions as well as reaction barriers and thermochemistry.

1.2.2 Density-Functional-Theory (DFT)

In DFT, the energy is computed based on the total electron density, which depends on three spatial coordinates regardless of the number of electrons. Kohn-Sham DFT, which is the form typically used for chemical applications, can be formulated as a modified form of Hartree-Fock theory in which the effects of exchange are replaced with an exchange-correlation potential. In theory, if the exact form of the exchange-correlation potential were known, DFT would yield exact solutions to the electronic Schrodinger equation (including effects of instantaneous electron-electron interactions), despite being an inherently mean-field approach.

The various DFT functionals (B3LYP, PBE, M06-2X, *etc*.) consist of different approximations to the exchange-correlation potential. Unfortunately, DFT methods do not provide a systematic way to converge to the exact solution of the Schrödinger equation. Moreover, commonly-used DFT functionals often contain empirical parameters, so a given DFT method can describe one class of molecules well but fail spectacularly for seemingly similar systems. Most DFT methods do not describe dispersion effects. As a result, empirical dispersion corrections are required in order to obtain reasonable results for weakly bound systems. Three DFT methods are routinely used by chemists to describe organic chemistry processes and materials: B3LYP, M06-2X and B97-D. Among these, B3LYP completely neglects dispersion, whereas M06-2X and B97-D capture dispersion to varying extents. These three functionals will be used in the course of the present work. Their differences will be contrasted in detail in future chapters.

1.2.3 Symmetry Adapted Perturbation Theory (SAPT)

Last, but not least, is symmetry-adapted perturbation theory, or SAPT. SAPT is designed to study non-covalent interactions. SAPT provides highly accurate interaction energies, and, in its lowest-order approximation (SAPT0), can be applied to systems up to a few hundred atoms. Additionally, SAPT provides individual contributions to the total interaction energy based on electrostatic, induction, dispersion, and exchange-repulsion effects. This can provide physical insight into the underlying factors that control the strength of a given non-covalent interaction, enhancing our understanding of individual non-covalent interactions. Such understanding can point towards ways of tuning the strength of these NCIs.

As with other computational methods, there are different levels of SAPT, corresponding to different levels of perturbation theory. Below, results using SAPT0 and SAPT2 are shown. By employing density fitting techniques, SAPT0 and SAPT2 can be applied to very large molecular systems. Further details about SAPT will be out of the scope of this dissertation but can be found in the references.

1.3 Basis Sets

For all of the methods described above, a basis set is required in order to mathematically describe the molecular orbitals. A basis set is a collection of simple functions for each atomic element that has been designed to provide accurate descriptions of MOs with a minimal number of functions. The expansion of each molecular orbital as a linear combination of basis functions provides a way to systematically vary the molecular orbitals in order to minimize the HF (or DFT) energy.

By including more basis functions, a better description of the MOs and a lower energy can be achieved; however the limitation in this particular case is the choice of method. For instance, even with very large basis set the HF wavefunction and energy are approximate solutions to the electronic Schrödinger equation and would not be an adequate choice for describing dispersion interactions. Early calculations were often done with Slater functions. However, these gave way to atom-centered Gaussian functions, which enable much more efficient evaluations of the required integrals. Currently, most molecular electronic structure computations are done with so-called split-valence basis sets, which allow description of tighter or looser electron distributions on atoms in different

environments. Common families of basis sets include Dunning-type and Pople-type basis sets, both of which can accommodate the addition of diffuse and/or polarization functions.

We use a number of common basis sets in this work, including the split-valence 6-31G(d) and 6-31+G(*d*,*p*) basis sets of Pople and co-workers, and the TZV*(2d,2p)* basis set. The latter basis set comprises Ahlrich's triple-ζ TZV basis set combined with the 2*d* and 2*p* polarization functions from the Dunning cc-pVTZ basis set for non-hydrogen elements and hydrogen, respectively. By means of these and other computational tools, the Wheeler research group focuses on the study of NCIs in the contexts of organocatalysis, organic electronic materials and protein-DNA interactions. In the present work, the computational studies of the roles of non-covalent interactions in both: organic reactions and organic materials are presented.

2. NON-COVALENT INTERACTIONS IN ORGANOCATALYSIS*

Computational methods have emerged as a powerful tool for modern organic chemistry.[10] In particular, DFT methods are now widely used among organic chemists to gain a more complete understanding of reaction mechanisms.[11] In the case or organocatalyzed reactions, careful computational analyses of the predicted transition state (TS) structures has helped in understanding observed enantiomeric excess (*ee*) results.[12-16] Computed TS geometries can also be used to refine and inform models for the mode of stereoinduction in these reactions, which can, in turn, form the basis for the rational design of improved catalysts.[17]

Ultimately, understanding the activity and selectivity of existing catalysts precedes the ability to effectively design new catalysts with improved performance.[18] It is to be expected that, with the increased number of methods and basis sets available, selecting a practical computational method that is consistent with experimental observations can become a daunting task. Often, the metric by which a given computational method is judged in applications to stereoselective reactions is the accuracy with which experimentally-determined *ee*'s can be reproduced. However, agreement between experimental *ee*'s and computational predictions does not guarantee that a method is reliable, or that it even identifies the correct TS structures. Moreover, in the case of reactions for which multiple pathways are operative, a given *ee* can be achieved in innumerable ways, and it is possible that some computational methods will predict accurate *ee*'s even from qualitatively incorrect

---

* Part of this chapter is reprinted with permission of The Royal Society of Chemistry. "Performance of DFT methods and origin of stereoselectivity in bipyridine N,N′-dioxide catalyzed allylation and propargylation reactions" by Sepulveda, Lu and Wheeler, 2014. Organic & Biomolecular Chemistry, Copyright 2014. http://pubs.rsc.org/en/content/articlelanding/2014/ob/c4ob01719f

predictions of relative reaction barriers or TS structures (*vide infra*). In such bases, conclusions drawn regarding details of given reaction can be incorrect. The ability of a computational method to predict the relative energies of *all* operative TSs, in addition to the overall stereoselectivity, is vital for a sound understanding of organocatalyzed reactions.

Below, we discuss computational studies of two reactions in which NCIs play key roles in stereoselectivy and chemoselectivity. In the first, we first present a benchmark study of a bipyridine *N*,*N*'-dioxide catalyzed alkylation reaction, and then explain why bipyridine *N*,*N*'-dioxide catalyzed allylation reactions general exhibit greater stereoselectivities than propargylations. Second, we present a preliminary study of a borate catalyzed hetero-Diels-Alder (HDA) reaction in which π-stacking interactions between the substrate and catalyst lead to pronounced selectivity for aromatic substrates over aliphatic substrates. In both cases, the proper description of both the underlying chemistry and operative NCIs is vital to achieving accurate predictions. Ultimately, the results provide insights into the origin of selectivity in these organocatalytic systems.

2.1 Bipyridine *N*,*N*'-dioxide Catalyzed Alkylation Reactions

2.1.1 Background

In order to assess the performance of some of the popular DFT methods employed routinely by organic chemists, we chose the bipyridine *N*,*N*'-dioxide of Nakajima and coworkers,[19-21] since it is one of the few known organocatalysts to work for both asymmetric allylation and propargylation reactions. Catalyst (*S*)-**1** reacts under similar conditions with either allyl or allenyl tricholorosilanes to afford enantioenriched alcohols, as depicted in Figure 2. However, the resulting stereoselectivity for propargylation reactions (52% *ee*) is noticeably less than that observed for allylations (88% *ee*), despite the outward similarity of

these two reactions. Our goal in this work is two-fold: 1) Assess the performance of DFT methods applied to these reactions in order to identify approaches that provide reliable predictions of relative barrier heights as well as stereoselectivities of these reactions; and 2) Explain the origin of stereoselectivity of allylations catalyzed by (*S*)-**1** as well as the reduced stereoselectivity in the case of propargylation reactions. This builds on our previous work[22,23] on bipyridine *N*-oxide catalysts for asymmetric alkylation reactions, and will also lay the groundwork for the computational design of bipyridine *N*,*N*'-dioxide catalysts for asymmetric propargylations.

Figure 2 Allylation and propargylation of benzaldehyde catalyzed by (*S*)-**1**

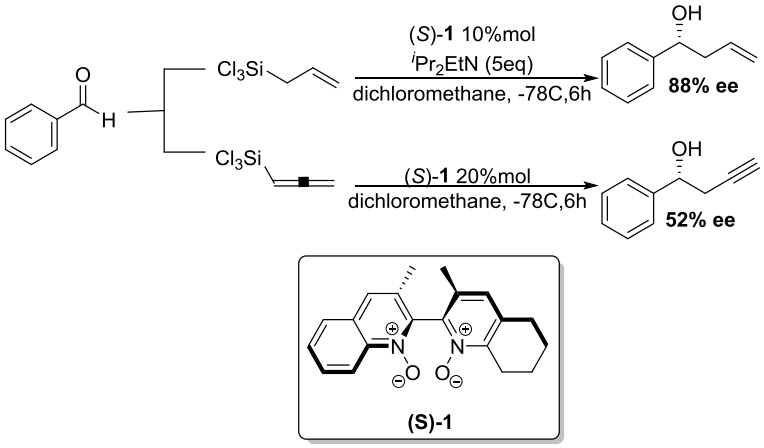

Asymmetric allylations and propargylations of aromatic aldehydes are key C-C bond forming transformations, providing access to chiral homoallylic and homopropargyllic alcohols, respectively. It is well-established that the asymmetric induction for these reactions can be achieved by means of chiral organocatalysts.[24,25] Historically, both Lewis acids and bases have been used, but only the latter have been shown to provide high degrees of setereoselectivity. Mechanistic studies of Kotora and coworkers[26,27] suggest that these

reactions can proceed by two different mechanisms, depending on the solvent used. Under Nakajima's conditions,[19-21] using dichloromethane as solvent, it is generally assumed that the reaction follows the dissociative route shown in Figure 3.[28] The stereocontrolling step involves a chair-like transition state featuring a hexacoordinate silicon, in which both alkyl−aldehyde and aldehyde−silicon bonds are formed, as originally proposed by Denmark and coworkers.[29-33]

Figure 3 Catalytic cycle for the alkylation of aryl aldehydes catalyzed by bidentate Lewis-basic catalysts (LB).

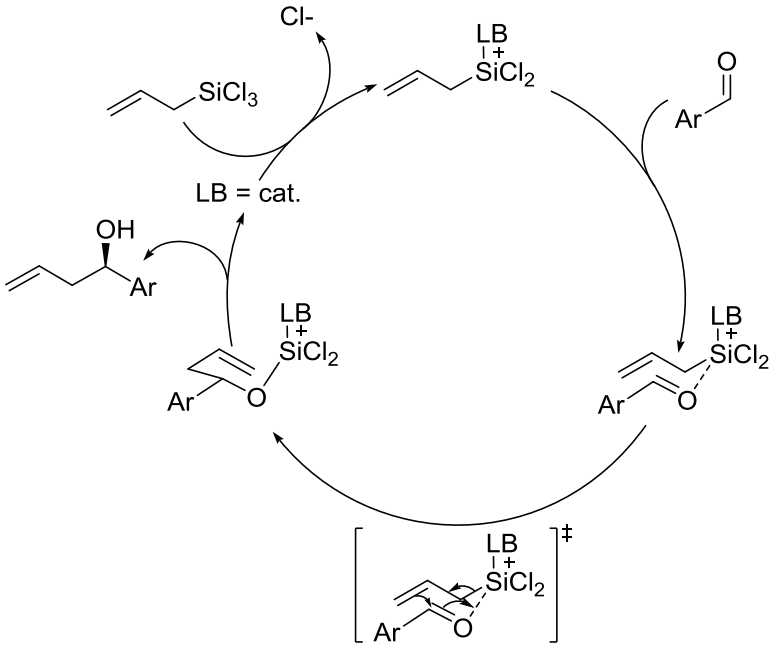

The well-organized coordination sphere around the silicon keeps the nucleophile, electrophile and organocatalyst in close proximity, providing a chiral environment through a rigid, chair-like transition state that is not achievable when using a chiral Lewis acid as

catalyst.[22,23,34] In the case of allylations catalyzed by (*S*)-**1**, Nakajima and co-workers[21] explained the observed stereoselectivity based on the transition state model depicted in Figure 4. This TS model was based in part on the observation that the stereoselectivity was independent of substitution at positions R_1 and R_2, but the *ee* was reduced to 49% in the presence of a methyl group at position R_3. This latter observation was rationalized by steric interactions between this methyl group and the aromatic walls of the catalyst.

Predicting the selectivity for these reactions requires precise predictions of the relative free energy barriers for this stereocontrolling transition state. In particular, it is vital that the lowest-lying (*R*) and (*S*) transition state structures be predicted accurately, as they are the primary determinants of the overall stereoselectivity. However, comparisons of computationally predicted stereoselectivities with experimental *ee*'s alone are insufficient to gauge the accuracy of a given computational method. This is because the prediction of a given *ee* can be achieved in innumerable ways. Below, we demonstrate some of the pitfalls encountered predicting correct enantioselectivities of organocatalyzed reactions by way of *N,N'*-dioxide catalyzed allylation and propargylation reactions while also explaining the origin of stereoselectivity allylations and propargylations catalyzed by (*S*)-**1**. The resulting TS model is qualitatively different from that proposed by Nakajima and co-workers,[21] but is consistent with our recent work on bipyridine *N*-oxide catalyzed alkylation reactions.[22,23] Together, these data provide key insights into the nature of bipyridine *N*,*N*'-dioxide catalyzed alkylation reactions, and pave the way for the rational design of more effective catalysts for both reactions.

Figure 4 (a) Transition state model of Nakajima and co-workers[21] to explain the (*R*)-stereoselectivity of (*S*)-**1** in the allylation of aromatic aldehydes. Key TS structures for the (b) allylation and (c) propargylation of benzaldehyde. Stabilizing 1,3-diaxial interactions present in **BP2**(*R*) are indicated with dashed arrows

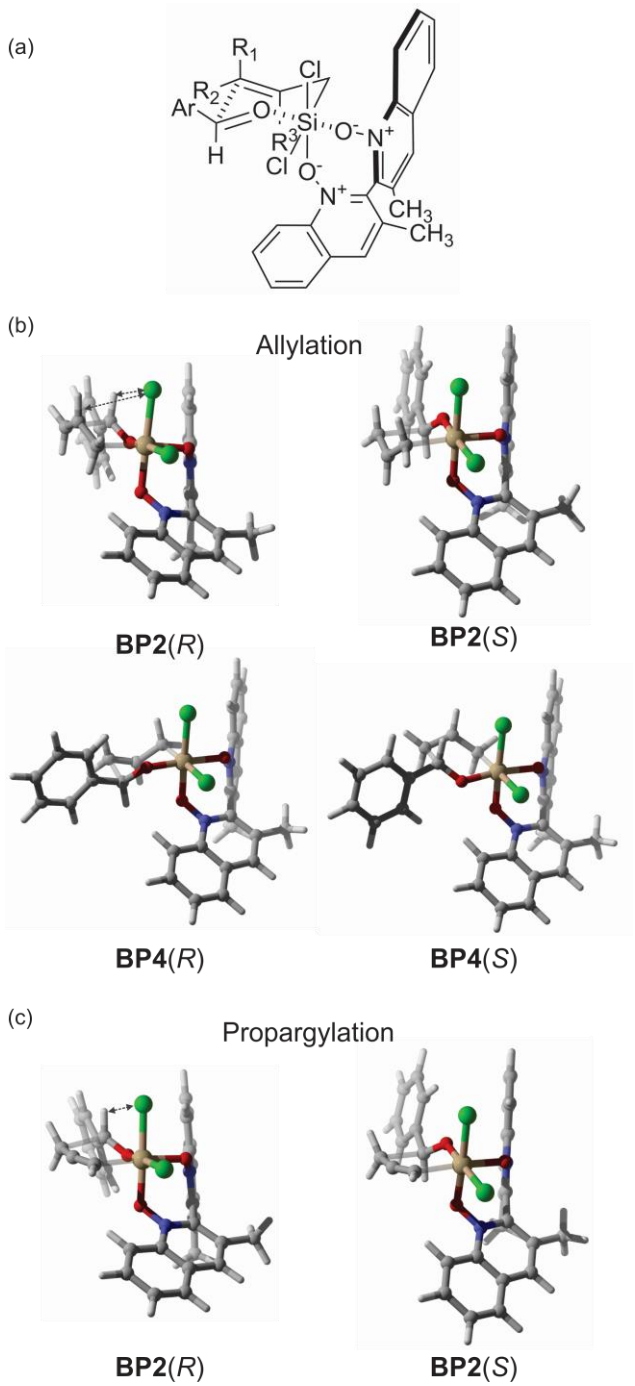

2.1.2 Computational Methods

Transition state geometries were optimized at four levels of theory, using different DFT functionals combined with commonly employed basis sets: B3LYP/6-31G (d),[35-38] M06-2x/6-31+G(*d,p*),[39] B97-D/TZV*(2d,2p)*[40-42] and ω-B97xD/TZV*(2d,2p)*.[43] These geometry optimizations used the PCM model[44,45] to account for solvent effects (dichloromethane). Frequency calculations were performed at the same level of theory as the optimizations. Transitions states were located using the Berny Algorithm[46,47] and characterized by the existence of a single imaginary vibrational frequency. *ee*'s were evaluated on the basis of solution-phase free energies using classical transition state theory (TST) and accounting for a Boltzmann distribution of possible transition states, as done previously for bipyridine *N*-oxide catalyzed alkylations.[22,23] Free energies (T = 195K) were evaluated based on partition functions derived from the rigid-rotor and harmonic oscillator approximations.

Gas-phase single point energies were evaluated at the B97-D/TZV*(2d,2p)* optimized TS geometries at the df-MP2/cc-pVTZ (density-fitted second-order Møller-Plesset perturbation theory with the cc-pVTZ basis set) and the LPNO-CEPA/1/def2-TZVP (local pair-natural orbital coupled electron pair approximation with the def2-TZVP basis set) levels of theory.[7-9,48] The latter method provides rigorous reference data against which the DFT energies were benchmarked.[49] For this purpose, gas-phase single point energies with the ωB97X-D, M06-2X, B2PLYP, B2PLYP-D, M05-2X, mPW1PW91, and B3LYP DFT functionals paired with 6-31G(d), 6-31+G(d,p), and TZV*(2d,2p)* basis sets were computed at the B97-D/TZV*(2d,2p)* optimized geometries. All DFT computations were done using

Gaussian09,[50] while Molpro[51] was used to compute df-MP2 energies and Orca 2.9.1[52] was used for the LPNO-CEPA computations.

2.1.3. Results and Discussion

We first determined the possible arrangements of the bidentate catalyst, aldehyde, and alkyl nucleophile around the hexacoordinate silicon. It is often assumed in the literature that for bipyridine *N*-oxide and *N*,*N*'-dioxide catalyzed alkylation reactions,[53,54] there is a single preferred ligand arrangement in which the chlorines adopt a *trans* arrangement and the alkyl nucleophile is located *trans* to an *N*-oxide (configuration **BP1** in Figure 5). However, Wheeler and co-workers[22,23] showed that, in the case of bipyridine *N*-oxides, there are ten feasible arrangements of ligands, given rise to twenty possible TS structures [ten leading to the (*R*)-alcohol, ten leading to the (*S*)-alcohol]. Moreover, depending on the catalyst, any of these ligand configurations can be low-lying.[22,23] Consequently, for bipyridine *N*-oxide catalyzed alkylation reactions, one must consider all of these possible pathways in computations. We assume that the same hold for bipyridine *N*,*N*'-dioxides catalyzed alkylations.

Figure 5 The five unique ligand configurations that are compatible with the alkylations of aromatic aldehydes catalyzed by C_2-symmetric bipyridine *N*,*N*'-dioxides. For each of the ligand configurations **BPX** (X = 1-5), there will be a pair of TS structures leading to the (*R*) and (*S*) alcohol, denoted **BPX**(*R*) and **BPX**(*S*), respectively. "Nu" refers to the alkyl nucleophile, which will be either an allyl group or allenyl group for allylations and propargylations, respectively.

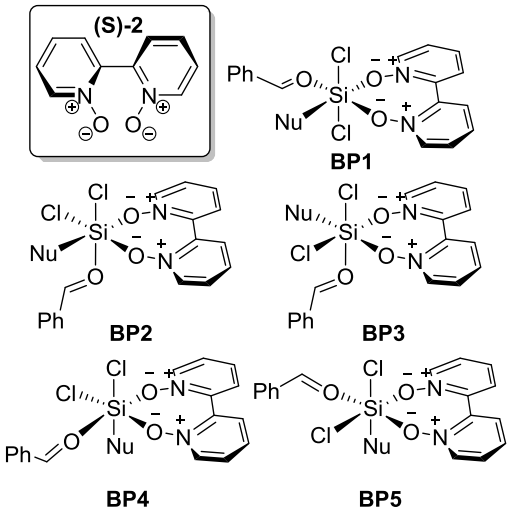

By analogy with the previous work of Wheeler and co-workers,[22,23] for C_2-symmetric bipyridine *N*,*N*'-dioxide catalyzed alkylations there are five possible arrangements of the alkyl nucleophile, aldehyde, and two chlorines around the hexacoordinate silicon that are compatible with the addition of the alkyl group to the aldehyde (see Figure 5). For each of these configurations, the alkyl group can add to the *Si* or *Re* face of the aldehyde, leading to formation of the (*S*)- or (*R*)-alcohol, respectively. Thus, for a given C_2-symmetric catalyst, one must consider ten possible TS structures—five leading to formation of the (*R*) alcohol [**BP1**(*R*) – **BP4**(*R*)], and five leading to the (*S*) alcohol [**BP1**(*S*) – **BP5**(*S*)]. Nakajima's proposed transition state (Figure 2) corresponds to **BP4**(*R*).[21]

All ten TS structures were located for both the allylation and propargylation of benzaldehyde catalyzed by (*S*)-**1** at six different levels of DFT theory: B97-D/TZV*(2d,2p)*,

B97-D/TZV*(2d,2p)*, ωB97X-D/TZV*(2d,2p)*, B3LYP/6-31G(*d*), B3LYP/TZV*(2d,2p)*, and M06-2X/6-31+G(*d,p*). Key TS structures are shown in Figure 4. The corresponding relative free energies are listed in Table 2, while the *ee*'s predicted from these relative free energies are listed in Table 3. Surprisingly, despite the structural similarities of the allylation and propargylation transition states, there was wide variation in predicted *ee*'s between these two reactions. In particular, the spread in predicted *ee*'s for the propargylation (0 to 99% *ee*) is significantly larger than that for the allylation (56 to 97% *ee*). Apparently, the stereoselectivity of the propargylation reaction is much more sensitive to theoretical method than the allylation.

Perhaps the most striking feature of the data presented in Table 2 is that, regardless of the level of theory, Nakajima's TS structure [**BP4**(*R*)] is significantly higher in free energy than the lowest-lying structure, **BP2**(*R*). Indeed, **BP4**(*R*) is among the least favorable TS structures, and will play no role in this reaction. This mirrors previous results[22,23] for bipyridine *N*-oxide alkylations catalysts,[55,56] for which proposed TS models corresponded to relatively high-lying TS structures. Moreover, as discussed more below, the ligand configuration corresponding Nakajima's TS model leads to the opposite stereoselectivity compared to the experimental observation. That is, **BP4**(*R*) is higher in free energy than **BP4**(*S*), even though the TS model of Nakajima was intended to explain the (*R*)-selectivity of (*S*)-**1**.

A number of interesting observations can be made from the data in Table 3 regarding the performance of these DFT methods for these two outwardly similar reactions. For example, we tested B97-D and B3LYP with two different basis sets, resulting in surprisingly different predicted *ee*'s. In particular, although B97-D/TZV*(2d,2p)* provides

stereoselectivities in general agreement with experiment for both the propargylation and allylation of benzaldehyde, when paired with the smaller 6-31G(*d*) basis set this functional predicts that **BP2**(*S*) is isoergonic with **BP2**(*R*). That is, B97-D/6-31G(d) predicts no stereoselectivity for the propargylation of benzaldehyde catalyzed by (*S*)-**1**. Although the B3LYP functional is somewhat less sensitive to basis set, it provides more sound predictions when paired with the larger TZV*(2d,2p)* basis set.

Table 2 Relative free energies (in kcal/mol) for the ten possible propargylation and propargylation transition states catalyzed by (*S*)-**1** using six levels of DFT theory, relative to the lowest-lying TS.

	(*R*) Transition States					(*S*) Transition States				
Method	**BP1**	**BP2**	**BP3**	**BP4**	**BP5**	**BP1**	**BP2**	**BP3**	**BP4**	**BP5**
					Allylation					
B97-D/TZV*(2d,2p)*	4.0	0.0	8.2	7.0	5.5	3.1	1.1	2.1	4.9	A
B97-D/6-31G(d)	4.8	0.0	8.3	7.8	5.3	4.3	0.5	2.0	5.3	A
ωB97X-D/TZV*(2d,2p)*	4.0	0.0	8.7	5.0	5.3	3.1	1.1	2.0	4.3	A
B3LYP/6-31G(d)	2.5	0.0	8.4	6.7	4.7	2.0	1.8	2.6	3.5	A
B3LYP/TZV*(2d,2p)*	1.2	0.0	7.8	6.4	3.9	0.9	1.6	2.1	3.2	A
M06-2X/6-31+G(*d*,*p*)	5.7	0.0	9.5	9.6	6.1	3.1	1.6	2.8	5.6	a
					Propargylation					
B97-D/TZV*(2d,2p)*	3.2	0.0	6.2	6.1	3.6	3.3	0.8	1.2	4.9	7.5
B97-D/6-31G(d)	3.8	0.0	5.9	6.0	2.9	4.1	0.0	1.1	5.5	7.6
ωB97X-D/TZV*(2d,2p)*	4.1	0.0	7.7	8.1	4.6	4.9	2.0	2.7	6.5	9.5
B3LYP/6-31G(d)	0.8	0.0	5.6	5.2	2.8	1.7	0.3	1.1	3.4	7.1
B3LYP/TZV*(2d,2p)*	0.4	0.0	5.6	5.5	2.7	1.4	0.6	2.5	3.5	7.2
M06-2X/6-31+G(*d*,*p*)	2.9	0.0	7.2	7.7	3.8	3.8	1.0	0.7	5.9	9.2

[a]For the allylation reaction, we were unable to locate TS structures corresponding to **BP5**(*S*) in which the bipyridine *N*,*N*'-dioxide maintained both bonds to the silicon. The resulting pentacoordinate structures were 9 to 19 kcal/mol higher in free energy than **BP2**(*R*).

Satisfyingly, all of the methods but one, ωB97X-D/TZV*(2d,2p)*, correctly predict that the propargylation reaction will be less stereoselective than the allylation; ωB97X-D/TZV*(2d,2p)* drastically overestimates the *ee* of the propargylation reaction. Moreover, other than B97-D/6-31G(*d*), all of the methods provide at least qualitatively corrected *ee*'s for both reactions, compared to experiment.

Table 3 Predicted Enantioselectivity for Allylation and Propargylation catalyzed by (*S*)-**1** at four levels of theory, along with the experimental values.

Method	Propargylation	Allylation
Experimental[19,21]	52	88
B97-D/TZV*(2d,2p)*	73	88
B97-D/6-31G(d)	0	56
ωB97X-D/TZV*(2d,2p)*	99	87
B3LYP/6-31G(d)	33	97
B3LYP/TZV*(2d,2p)*	73	81
M06-2X/6-31+G(*d,p*)	61	96

Unfortunately, despite most of these methods predicting *ee*'s in reasonable agreement with experiment (Table 3), the underlying relative free energies for the ten possible transition states are drastically different (see Table 2). For example, for the allylation reaction, B3LYP/TZV*(2d,2p)* predicts that **BP1**(*S*) will be the lowest-lying TS structure leading to the (*S*)-alcohol. This is in stark contrast to the other levels of theory tested, which predict that **BP2**(*S*) will be lowest-lying among the (*S*) transition states. Similarly, while all of the other methods predict that **BP2**(*S*) will be at least 1 kcal/mol higher in free energy than **BP2**(*R*), B97-D/6-31G(d) predicts **BP2**(*S*) to lie only 0.5 kcal/mol higher in free energy than **BP2**(*R*). These differences are important in developing models of the stereoselectivity of these

reactions, since such models depend on the identification of the correct low-lying (*R*) and (*S*) transition states.

Differences among predicted free energies for the low-lying TS structures are even more severe for the propargylation reaction. For example, B3LYP/6-31G(d) predicts **BP1**(*R*) for the propargylation of benzaldehyde is only 0.8 kcal/mol higher in free energy than **BP2**(*R*), whereas the other methods predict **BP1**(*R*) to be at least 2.9 kcal/mol higher in free energy than **BP2**(*R*). When paired with the larger TZV*(2d,2p)* basis set, B3LYP predicts **BP1**(*R*) to be only 0.4 kcal/mol higher in free energy than **BP2**(*R*). Again, these differences will impact our understanding of the origin of stereoselectivity for this reaction. In particular, according to B3LYP, **BP1**(*R*) will contribute formation of the (*R*) alcohol, while the other functionals rule out the involvement of this particular pathway. Overall, B3LYP predicts the TS structures that feature a *trans*-Cl ligand arrangement (**BP1**) to lie much lower in free energy, relative to the other TS structures, than the other functionals tested. Intrigingly, this ligand configuration is often assumed to be the favored one for these reactions.[53,54]

Unfortunately, there is no way to gauge the ability these functionals to identify the low-lying TS structures for these reactions solely based on the overall *ee*'. Instead, we must directly assess the performance of these functionals for the relative energies of the individual TS structures. This will be vital in order to identify DFT methods that correctly identify the lowest-ing (*R*) and (*S*) transition state structures.

2.1.3.1 Computational Benchmark

To provide a more nuanced assessment of the accuracy of various DFT functionals for these ten TS energies, we computed gas-phase single-point energies using a wider range of DFT functionals: B3LYP, B97-D, M06-2X, M05-2X, mPW1PW91 and ωB97X-D. For each of these functionals, we considered three basis sets: 6-31G(*d*), 6-31+G(*d,p*) and TZV*(2d,2p)*. All of these single point energies were evaluated at the B97-D/TZV*(2d,2p)* optimized geometries, in order to differentiate between geometry-based errors and inherent errors in the underlying electronic energies. Moreover, the consideration of gas-phase energies allows us to compare against high-level LPNO-CEPA/1 results. The assumption is that the variation in relative free energies observed in Table 2 results from differences in the underlying electronic energies, not solvent or free energy corrections.

Table 4 shows LPNO-CEPA/1 energies for the allylation transition states, relative to **BP2**(*R*), along with the *errors* in the relative energies from MP2 and eight different DFT functionals paired with three different basis sets. Analogous data for the propargylation reaction are shown in Table 5. The DFT predicted relative energies show a troubling degree of variation, with many predictions in error by nearly 5 kcal/mol compared to the LPNO-CEPA/1 benchmark.

Table 4. LPNO-CEPA/1 energies (kcal/mol) for the ten TS structures for the allylation reaction, relative to the lowest-lying structure **BP2**(*R*), along with errors in these relative energies from MP2 and eight DFT functionals compared to the LNPO-CEPA/1 results.

Method	**BP1**	**BP2**	**BP3**	**BP4**	**BP5**	**BP1**	**BP2**	**BP3**	**BP4**	**BP5**		
	(*R*) Transition States					(*S*) Transition States						
LPNO-CEPA/1	2.9	0.0	11.5	13.8	7.7	2.8	5.1	3.3	7.7	10.4	Mean Error	Max Error
MP2	-1.2	0.0	-0.7	-1.6	-0.9	-1.3	-1.1	-0.5	-1.1	0.9	-0.8	1.6
						6-31G(d)						
ωB97X-D	-0.1	0.0	-2.0	-1.1	-1.2	-0.3	-1.5	-1.0	-0.8	-1.0	-0.9	2.0
M06-2X	-1.3	0.0	-2.5	-1.0	-1.2	-1.8	-0.9	-1.2	-1.1	3.4	-0.7	2.5
M05-2X	-1.8	0.0	-2.3	-1.3	-1.4	-2.2	-0.7	-1.2	-1.6	2.4	-1.0	2.3
B2PLYP-D	-0.5	0.0	-2.3	-2.2	-1.6	-0.5	-1.5	-1.4	-1.7	-1.3	-1.3	2.3
B2PLYP	-2.6	0.0	-2.6	-3.6	-2.8	-2.6	-1.3	-1.3	-3.1	-3.4	-2.3	3.6
B97-D	-0.3	0.0	-2.9	-3.3	-1.7	-0.3	-1.9	-1.5	-1.9	-3.9	-1.8	3.9
mPW1PW91	-3.9	0.0	-3.2	-4.3	-3.7	-4.1	-0.9	-1.5	-4.2	-3.6	-2.9	4.3
B3LYP	-4.4	0.0	-3.6	-5.1	-3.9	-4.4	-1.1	-1.6	-4.4	-4.4	-3.3	5.1
						6-31+G(d,p)						
ωB97X-D	-0.1	0.0	-2.0	-1.0	-0.8	-0.2	-1.4	-0.8	-0.7	-1.1	-0.8	2
M06-2X	-1.1	0.0	-2.3	-0.6	-0.5	-1.5	-0.9	-0.8	-0.7	3.7	-0.5	2.3
M05-2X	-1.8	0.0	-2.3	-1.0	-0.8	-2.0	-0.7	-0.8	-1.3	2.7	-0.8	2.3
B2PLYP-D	-0.5	0.0	-1.9	-1.7	-0.3	-0.4	-1.7	-0.7	-0.9	0.0	-0.8	1.9
B2PLYP	-2.5	0.0	-2.2	-3.0	-1.6	-2.4	-1.6	-0.6	-2.3	-2.1	-1.8	3
B97-D	-0.6	0.0	-3.2	-3.5	-1.6	-0.6	-1.8	-1.4	-2.1	-4.2	-1.9	4.2
mPW1PW91	-4.1	0.0	-3.4	-4.4	-3.4	-4.2	-0.8	-1.3	-4.2	-3.6	-2.9	4.4
B3LYP	-4.7	0.0	-3.8	-5.3	-3.7	-4.7	-1.0	-1.4	-4.6	-4.9	-3.4	5.3
						TZV*(2d,2p)*						
ωB97X-D	-1.0	0.0	-2.3	-1.8	-1.6	-1.1	-1.3	-1.2	-1.4	-2.6	-1.4	2.6
M06-2X	-2.2	0.0	-2.6	-1.4	-1.5	-2.6	-0.5	-1.2	-1.7	2.1	-1.2	2.6
M05-2X	-2.7	0.0	-2.4	-1.7	-1.6	-3.0	-0.4	-1.2	-2.0	1.4	-1.4	3.0
B2PLYP-D	-1.4	0.0	-2.2	-2.4	-1.5	-1.5	-1.1	-1.3	-1.9	-1.5	-1.5	2.4
B2PLYP	-3.5	0.0	-2.5	-3.7	-2.7	-3.5	-0.9	-1.3	-3.3	-3.6	-2.5	3.7
B97-D	-1.3	0.0	-3.3	-3.9	-2.2	-1.3	-1.6	-1.7	-2.5	-5.2	-2.3	5.2
mPW1PW91	-5.0	0.0	-3.5	-5.1	-4.2	-5.1	-0.6	-1.7	-4.9	-5.1	-3.5	5.1
B3LYP	-5.3	0.0	-3.8	-5.7	-4.2	-5.4	-0.8	-1.6	-5.0	-6.0	-3.8	6.0

Table 5. LPNO-CEPA/1 energies (kcal/mol) for the ten TS structures for the propargylation reaction, relative to **BP2**(*R*), along with errors in these relative energies from MP2 and eight DFT functionals compared to the LNPO-CEPA/1 results.

Method	**BP1**	**BP2**	**BP3**	**BP4**	**BP5**	**BP1**	**BP2**	**BP3**	**BP4**	**BP5**		
	(*R*) Transition States					(*S*) Transition States						
LPNO-CEPA/1	2.8	0.0	10.0	11.4	6.2	3.7	2.5	13.2	8.2	2.9	Mean Error	Max Error
MP2	-1.2	0.0	-0.9	-1.5	-1.6	-1.3	-0.5	-1.3	-1.2	-0.7	-1.0	1.6
						6-31G(d)						
ωB97X-D	-0.4	0.0	-1.8	-1.4	-1.7	-0.4	-1.2	-1.5	-0.8	-1.5	-1.1	1.8
M06-2X	-1.8	0.0	-2.1	-1.5	-2.1	-1.5	-1.0	-0.9	-1.3	-1.8	-1.4	2.1
M05-2X	-2.2	0.0	-2.3	-1.8	-2.0	-2.0	-0.7	-1.0	-1.6	-1.8	-1.5	2.3
B2PLYP-D	-0.8	0.0	-2.3	-2.5	-2.2	-0.8	-1.0	-1.9	-1.9	-2.1	-1.5	2.5
B2PLYP	-0.7	0.0	-3.2	-3.3	-2.3	-0.8	-1.1	-3.1	-2.1	-2.4	-1.9	3.3
B97-D	-2.6	0.0	-2.6	-3.8	-2.7	-2.9	-0.9	-3.0	-3.3	-1.6	-2.3	3.8
mPW1PW91	-4.1	0.0	-3.4	-4.9	-3.3	-4.4	-0.9	-3.5	-4.3	-1.7	-3.0	4.9
B3LYP	-4.5	0.0	-3.7	-5.3	-3.1	-4.8	-0.8	-4.1	-4.6	-1.8	-3.3	5.3
						6-31+G(d,p)						
ωB97X-D	-0.2	0.0	-1.7	-1.4	-1.1	-0.3	-1.0	-1.4	-0.7	-1.1	-0.9	-1.7
M06-2X	-1.4	0.0	-1.9	-1.2	-1.4	-1.3	-0.7	-0.7	-0.9	-1.2	-1.1	-1.9
M05-2X	-1.9	0.0	-2.2	-1.6	-1.3	-1.9	-0.5	-0.7	-1.3	-1.2	-1.3	-2.2
B2PLYP-D	-0.5	0.0	-1.8	-1.9	-0.8	-0.7	-0.8	-1.1	-1.1	-1.1	-1.0	-1.9
B2PLYP	-0.9	0.0	-3.5	-3.6	-2.0	-1.1	-0.9	-3.2	-2.4	-2.1	-2.0	-3.6
B97-D	-2.3	0.0	-2.2	-3.2	-1.3	-2.7	-0.7	-2.1	-2.5	-0.7	-1.8	-3.2
mPW1PW91	-4.2	0.0	-3.5	-4.9	-2.8	-4.5	-0.7	-3.5	-4.4	-1.3	-3.0	-4.9
B3LYP	-4.8	0.0	-3.8	-5.5	-2.8	-5.2	-0.6	-4.2	-4.9	-1.4	-3.3	-5.5
						TZV*(2d,2p)*						
ωB97X-D	-1.1	0.0	-1.7	-1.9	-1.7	-1.2	-0.8	-2.1	-1.3	-1.3	-1.3	2.1
M06-2X	-2.5	0.0	-2.0	-1.9	-2.2	-2.3	-0.6	-1.3	-1.7	-1.5	-1.6	2.5
M05-2X	-2.8	0.0	-2.2	-2.1	-1.8	-2.8	-0.3	-1.3	-1.9	-1.5	-1.7	2.8
B2PLYP-D	-1.6	0.0	-2.0	-2.4	-1.9	-1.6	-0.5	-2.2	-2.0	-1.8	-1.6	2.4
B2PLYP	-3.8	0.0	-3.3	-3.8	-2.4	-1.8	-1.6	-0.6	-2.7	-2.3	-2.2	3.8
B97-D	-3.4	0.0	-2.3	-3.8	-2.4	-3.7	-0.4	-3.2	-3.4	-1.4	-2.4	3.8
mPW1PW91	-5.0	0.0	-3.4	-5.5	-3.3	-5.4	-0.4	-4.2	-4.9	-1.6	-3.4	5.5
B3LYP	-5.3	0.0	-3.7	-5.7	-3.1	-5.8	-0.4	-4.7	-5.1	-1.6	-3.5	5.8

Interestingly, all DFT functionals underestimate the energy of the other TS structures relative to **BP1**(*R*). Indeed, B3LYP, B2PLYP, and mPW1PW91 all predict **BP1**(*R*) to lie lower in energy than any of the other TS structures! However, we see that LPNO-CPEA/1 predicts that **BP1**(*R*) lies 2.9 and 2.8 kcal/mol higher in energy than **BP2**(*R*) for the allylation and propargylation reactions, respectively. Thus, from this data it appears that B3LYP is providing the correct *ee* for the propargylation reaction despite inaccurate underlying TS energies. Overall, we find that ωB97X-D/TZV*(2d,2p)* provides results in closest agreement with the LPNO-CEPA/1 benchmark values. Indeed, ωB97X-D/TZV*(2d,2p)* performs at least as well as MP2/aug-cc-pVTZ. M06-2X/6-31+G(d,p) also provides relative energies in excellent agreement with the LPNO-CEPA benchmark.

In light of the excellent performance ωB97X-D/TZV*(2d,2p)* with regard to the relative gas phase energies of the ten TS structures for the propargylation of benzaldehyde, it is rather surprising that ωB97X-D/TZV*(2d,2p)* drastically overestimates the ee for the propargylation reaction (see Table 3). B97-D/TZV*(2d,2p)*, on the other hand, does a mediocre job predicting relative energies of these TS structures. However, it does very well predicting the relative energies of the lowest-lying TS structures, which underlies its ability to provide reliable predictions of the *ee*'s. Moreover, because B97-D is a pure DFT functional, it can be used with density-fitting techniques that make it quite computationally efficient. Even though B3LYP also provided sound predictions for **BP2**(*S*) relative to **BP2**(*R*), the drastic overstabilization of **BP1**(*R*) and **BP1**(*S*) spoils its ability to properly identify the operative TS structures for these reactions. Overall, for our purposes, M06-2X/6-31+G(d,p) and B97-D/TZV*(2d,2p)* offer the ideal compromise between accuracy for key

transition states and sound predictions of overall stereoselectivities, and will be used in future work to predict stereoselectivities of bipyridine *N,N*'-dioxide catalyzed alkylation reactions.

2.1.3.2 Origin of Stereoselectivity of (*S*)-**1**

Having established that B97-D/TZV*(2d,2p)* provides sound predictions of both the overall stereoselectivity of bipyridine *N,N*'-dioxide catalyzed alkylation reactions (compared to experiment) and relative energies of the low-lying transition states (compared to computational benchmarks), we return to the origin of stereoselectivity in allylations and propargylations catalyzed by (*S*)-**1**, as well as the question of why catalyst (*S*)-**1** provides greater stereoselectivity in the case of the allylation compared to the propargylations. Nakajima *et al*.[21] explained the stereoselectivity of (*S*)-**1** based on the TS model depicted in Figure 3. However, as noted above, the ligand configuration corresponding to this TS model is not only much higher in free energy than other ligand configurations, but predicts the wrong stereoselectivity. Instead, the stereoselectivity of (*S*)-**1** for the allylation of benzaldehyde arises from the 1.1 kcal/mol gap in free energy between **BP2**(*R*) and **BP2**(*S*) (see Figure 4). This free energy difference can be explained by simple electrostatic interactions between the C-H bonds of the aldehyde and allyl group and the axial chlorine. In particular, in the lower-lying **BP2**(*R*), there are favorable 1,3-diaxial interactions between two C-H bonds and one of the chlorines. These interactions are absent in in **BP2**(*S*). Indeed, for all five (*R*, *S*) pairs of TS structures, the lower lying structure is always the one in which these two C-H bonds are aligned with one of the chlorines. This was observed previously for bipyridine *N*-oxide catalyzed allylations,[23] and appears to be a general source of enantiodifferentiation in these reactions. Qualitatively, these stabilizing electrostatic

interactions can be understood in terms of favorable alignment of the local dipoles of the C-H and Si-Cl bonds. This model is similar in spirit to previous explanations of the *E*/*Z* selectivity in the addition of allylboronates to aldehydes from Hoffmann and Landmann.[57]

The reduced stereoselectivity in the case of the propargylation catalyzed by (*S*)-**1**, compared to the allylation, stems from the 0.8 kcal/mol free energy difference between **BP2**(*R*) and **BP2**(*S*) for this reaction. That this free energy difference is smaller than the corresponding difference for the allylation reaction simply reflects the lack of a central C-H bond in the allenyl group. That is, in the allylation reaction there are two C-H bonds that can engage in favorable 1,3-diaxial interactions with the Cl, whereas there is only one in the propargylation reaction.

Finally, we note that Nakajima's TS model was based in part on the observation that methyl substitution at position R_3 lead to reduced *ee*'s. This was attributed to steric interactions between this methyl group and the catalyst. Instead, the reduced selectivity in this case stems from the removal of the central C-H bond in the allyl group. Indeed, the selectivity for the allylation reaction in which R_3 = Me (49% *ee*)[21] is commensurate with the 52% *ee* reported for the propargylation by (*S*)-**1**. In both cases, the reduced stereoselectivity arises from a lack of hydrogen at this central position on the alkyl group.

2.1.3.3 Inherent Stereoselectivities of Bipyridine *N*,*N*'-Dioxides

Following previous work by Wheeler and co-workers,[22,23] we next turn to bipyridine *N*,*N*'-dioxide [(*S*)-**2**] as a model catalyst in order to gain more general insight into the stereoselectivity of bipyridine *N*,*N*'-dioxides in asymmetric alkylations (see Figure 5). This simple model system enables the study of the inherent stereoselectivity of these different

ligand arrangements in the absence of other catalyst components. Table 6 shows the predicted relative free energies barriers for the ten possible TS structures for the allylation and propargylation of benzaldehyde catalyzed by (*S*)-**2**, along with the difference between the two barriers leading to the two enantiomeric alcohols.

Table 6. B97-D/TZV*(2d,2p)* predicted relative free energy barriers for the formation of the R and S alcohol for (*S*)-**2** catalyst, along with the difference in the free energies for the R and S pathways, all in kcal/mol

	Allylation			Propargylation		
	R	*S*	Diff.	*R*	*S*	Diff.
BP1	2.1	2.0	0.1	1.2	1.2	0.0
BP2	0.0	1.1	-1.1	0.0	0.4	-0.4
BP3	6.6	2.2	4.4	5.8	1.7	4.1
BP4	5.6	4.1	1.5	4.5	4.1	0.4
BP5	5.0	8.4	-3.4	2.8	3.5	-0.7

First, for this model system, **BP2**(*R*) is low-lying for both the allylation and propargylation reaction, as observed for (*S*)-**1**. Furthermore, **BP2**(*S*) is 1.1 and 0.4 kcal/mol higher in free energy than **BP2**(*R*) for the allylation and propargylation, respectively, which is consistent with the results for (*S*)-**1**. In particular, for Nakajima's catalyst (*S*)-**1**, we also found that **BP2**(*R*) was low-lying, with **BP2**(*S*) 1.1 and 0.8 kcal/mol higher in free energy. Interestingly, the present data predict that the model catalyst (*S*)-**2** will provide stereoselectivities equal to that for Nakajima's catalyst (*S*)-**1** for the allylation of benzaldehyde! This provides further evidence that the stereoselectivity of (*S*)-**1** for allylation reactions stems primarily from the electrostatic interactions with the chiral electrostatic environment of the hexacoordinate silicon, and not other interactions between the catalyst

and substrate. Overall, the general agreement between relative free energies for the model catalyst (*S*)-**2** and real catalyst (*S*)-**1** suggests that (*S*)-**2** can provide a proxy for more complex catalysts. Whether the results from (*S*)-**2** can be generalized to a broader range of bipyridine *N*,*N*'-dioxide based catalysts will be addressed in future work.

Interestingly, for the allylation reaction catalyzed by (*S*)-**2**, there is at least a 2 kcal/mol difference in free energy between **BP2** and the other four possible configurations. This suggests that, unlike for bipyridine *N*-oxide catalyzed alkylations,[24,25] it might be safe to consider only this ligand configuration when predicting stereoselectivities for bipyridine *N*,*N*'-dioxide catalyzed allylations. Of course, for some catalysts there could be significant steric (or other) interactions that render a different ligand configuration lower-lying. However, for the analogous propargylation reaction, the possible TS structures are much more closely packed energetically. In this case, it is necessary to consider at least several, if not all five, of the possible ligand configurations when predicting stereoselectivities.

More to the point, we see that for allylations catalyzed by bipyridine *N*,*N*'-dioxides, all but one of the ligand configurations (**BP1**) leads to significant gaps in free energy between the (*R*) and (*S*) transition states, even in the absence of other chiral components of the catalyst. That is, many of these ligand configurations lead to stereoselectivity merely through the impact of the chiral environment of the hexacoordinate silicon. This was observed previously for bipyridine *N*-oxide catalyzed alkylations by Wheeler and co-workers,[22] and underscores the importance of electrostatic interactions between the C-H of the aldehyde and one of the chlorines bound to the silicon. Consistent with these previous results, we once again find that the lower-lying TS structure for a given ligand arrangement always features a geometry with the aldehyde C-H pointing towards a chlorine, whereas the

ligand arrangements with the C-H pointing away from the Cl are always higher in energy. The lack of a significant free energy gap between **BP1**(*R*) and **BP1**(*S*) can be explained by the *trans* arrangement of the chlorines. In this case, the C-H is directed towards a chlorine in both **BP1**(*R*) and **BP1**(*S*).

For the propargylation reactions, this inherent stereoselectivity is greatly reduced—for a given ligand arrangement, the free energy gap between the (*R*) and (*S*) TS structures is less for the propargylation reaction than for the allylation reaction. That is, propargylation reactions are inherently less stereoselective than allylations. Again, this mirrors previous results for bipyridine *N*-oxides from Lu, Porterfield, and Wheeler,[23] and reflects the lack of a central C-H bond in the allenyl group. Ultimately, the present results suggest that highly stereoselective catalysts for the propargylation of benzaldehyde can be built on a bipyridine *N*,*N*'-dioxide scaffold by devising a catalyst that steers the reaction towards the highly inherently stereoselective ligand arrangement **BP3**, while blocking access to the other, less stereoselective ligand arrangements. Alternatively, a stereoselective bipyridine *N*,*N*'-dioxide propargylation catalyst can be designed by introducing non-covalent interactions that preferentially stabilize **BP2**(*R*) over **BP2**(*S*). Both strategies for propargylation catalyst design are currently being pursued, building on the present results.

2.1.4. Summary and Conclusions

Computational quantum chemistry can provide a powerful tool for understanding the origin of stereoselectivity in organocatalyzed reactions, and, ultimately, in the rational design of new catalysts. However, this requires methods that faithfully predict the operative transition state structures. We assessed the performance of several popular DFT functionals for the prediction of stereoselectivities for the allylation and propargylation of benzaldehyde

catalyzed by Nakajim's bipyridine *N*,*N*'-dioxide, (*S*)-**1**. Satisfyingly, most of these functionals predict *ee*'s in qualitative agreement with experiment. Unfortunately, this agreement with experiment appears to be fortuitous in some cases, since some of these functionals predict the incorrect low-lying TS structures. For example, B3LYP/TZV*(2d,2p)* predicts the wrong transition state for formation of the (*S*)-alcohol in the allylation reaction, despite predicting an overall *ee* in excellent agreement with experiment (81% vs 88%). These data should serve as a warning that the reproduction of experimental *ee*'s along is insufficient to guarantee the performance of a given computational method. Moreover, several methods tested performed significantly better for allylations than propargylations, despite the outward similarity of these two reactions. In particular, B97-D/6-31G(d) fails to predict any stereoselectivity for the propargylation of benzaldehyde catalyzed by (*S*)-**1**, despite providing a reasonably accurate *ee* for the corresponding allylation reaction. Overall, of the DFT methods tested here, M06-2X/6-31+G(d,p) and B97-D/TZV*(2d,2p)* seem to provide the best compromise of accuracy for individual TS structures and overall predictions of stereoselectivites. Even though the errors in B97-D predicted relative energies are large overall, this functional provides accurate energies for the lowest-lying TS structures and is able to provide reliable predictions of stereoselectivities of allylations and propargylations catalyzed by bipyridine *N*,*N*'-dioxides. B97-D and M06-2X offer the added advantage of providing accurate descriptions of the NCIs that underlie the stereoselectivity and activity of many organocatalysts.

We also examined the origin of stereoselectivity in allylations and propargylations catalyzed by (*S*)-**1**. Ultimately, we showed that favorable 1,3-diaxial interactions between C-H bonds on the aldehyde and allyl group and one of the chlorines underlie the

stereoselectivity in allylation reactions. Moreover, the relative lack of stereoselectivity in *N*,*N*'-dioxide catalyzed propargylations arises from the lack of a central C-H bond in the allenyl group. Unforunately, Nakajima's transition state model (Figure 3) is based on the incorrect arrangement of ligands surrounding the hexacoordinate silicon. Moreover, the ligand configuration featured in Nakajima's TS model actually leads to preferential formation of the (*S*)-alcohol, in contrast with the experimental observation of formation of the (*R*)-alcohol in 88% *ee*. This is because the ligand configuration in Nakajima's TS model (**BP4**) is inherently selective for formation of the (*S*)-alcohol.

Unlike bipyridine *N*-oxide catalyzed allylation reactions, for *N*,*N*'-dioxide catalyzed allylations we found that a single ligand configuration (**BP2**) that is favored over the others and is likely operative in all bipyridine *N*,*N*'-dioxide catalyzed allylations. On the other hand, for bipyridine *N*,*N*'-dioxide catalyzed propargylation reactions, transition states arising from the five possible ligand configurations are much more closely spaced energetically. Consequently, several different ligand configurations could come into play in these reactions, as was seen for bipyridine *N*-oxide catalyzed reactions.[22,23] Ultimately, the present results point towards two viable strategies for the rational design of bipyridine *N*,*N*'-dioxide catalysts for asymmetric propargylations. These strategies are currently being pursued, and will be discussed in a forthcoming publication.

2.2 A Lewis – Acid – Catalyzed HDA Reaction: Quantifying the Role of NCIs in a Cage-Shape Borate Catalyst

2.2.1 Background

As mentioned in the Introduction, many of the NCIs in Figure 1 have been proved useful in the development of more active and selective organocatalysts. For the purposes of this chapter, particular interest will be paid to dispersion-dominated interactions, such as π-stacking interactions. Experimentally, the contribution of these various non-covalent interactions to organocatalytic activity requires the synthesis of multiple catalysts or derivatives and measuring the resulting catalytic activity. Such studies can be complemented by results from computational chemistry, which can provide a more direct view of the geometries and interactions occurring throughout the reactions. The latter is very important, since, for the most part, only qualitative information can be obtained experimentally about the role of specific NCIs in bigger molecules.

In the present chapter, DFT methods that provide accurate descriptions of NCIs are used to identify and quantify the role of NCIs in the selectivity of an organocatalyzed hetero-Diels-Alder reaction. Specifically, the work of Baba and coworkers[58] is taken as an example of a process where NCIs play a significant role in chemoselectivity. Baba et al. recently reported the synthesis of a series of cage-like borate catalysts for hetero-Diels-Alder reactions[58] that combine the reactivity of a Lewis acid and the structural features of clathrates. In addition, Baba's research group found that these catalysts were able to discriminate between aliphatic and aromatic aldehydes through molecular recognition.

The hetero-Diels-Alder (HDA) reaction is one of the most extensively used reactions in organic chemistry, because it provides access to substituted heterocycles in a

stereospecific fashion. It is a thermally allowed [4+2] cycloaddition in which either the diene or dienophile can contain a hetero atom.

For this reaction to proceed with a low barrier, the HOMO of the diene and the LUMO of the dienophile should have good overlap. This is typically achieved by pairing an electron-rich diene with an electron-poor dienophile. A widely used electron-rich diene is Danishefsky's diene (DD, see Figure 6a) which has been used for improving the reactivity of some dienes towards very non-reactive dienophiles. Additionally, it provides easy access to the formation of a carbon-carbon and a carbon-oxygen bond that can be further exploited in the synthesis of dihydropyrone-containing natural products.

HDA reactions can be further accelerated through the use of Lewis acid catalysts. For organocatalyzed reactions where no transition metals are being used, group 13 metal compounds (ML_3) are one of the most important classes of Lewis acids due to their vacant p-orbitals.[59] For the present work, boron will be the metal of interest, since the vacant p-orbital's energy is relatively close to the one of carbon, oxygen, nitrogen, etc.

Figure 6 (a) HDA reaction between Danishefsky's diene and aldehydes; (b)Increased Lewis acidity in constrained borate catalysts as shown by HOMO - LUMO gap

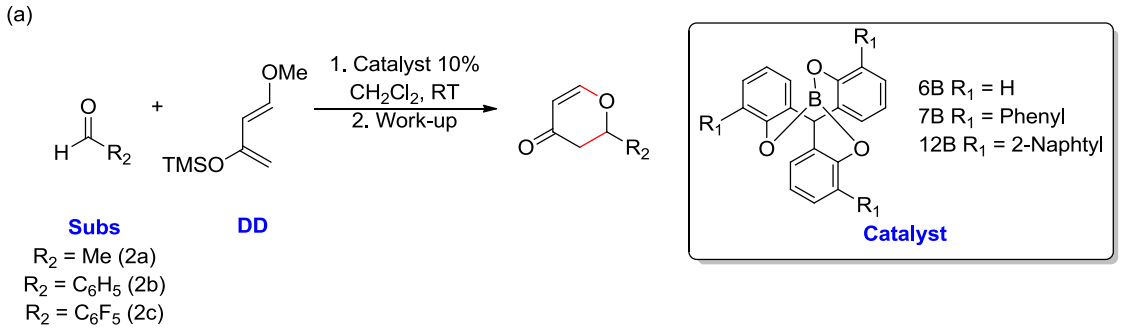

Figure 6 Continued

(b)

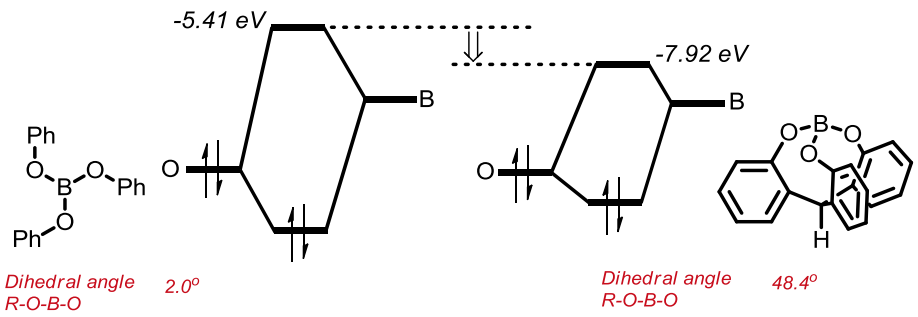

Baba and coworkers[59] have shown that the effectiveness of boron-based Lewis acids can be further enhanced by changing the geometry around the boron in order to favor the availability of the vacant p-orbital. In 2006, Baba and co-workers[58] reported the synthesis of cage-shaped borates that exhibited higher catalytic activity when used in a HDA reaction, as compared to normal, planar borates. This increased catalytic activity can be accounted for by the increased Lewis acidity arising from the geometric constraints that modifies the HOMO-LUMO gap, as shown in Figure 6b. The later was confirmed by DFT calculations.[59,60] The search for more efficient Lewis acid catalysts that can be used in the HDA reaction represents an active area of research, as demonstrated not only by the work of Baba, but also recent work from Masson and List.[61]

In 2011, Baba's group reported that cage-shaped borate catalysts 7B and 12B (Figure 6a) selectively catalyze the HDA reaction of aromatic over aliphatic aldehydes.[58] Catalyst 6B, on the other hand, does not provide such selectivity. It was proposed that stabilizing π-stacking interactions between the aromatic aldehyde and the π-pocket of catalysts 7B and 12B were responsible for the selectivity. Chiral boron catalysts have previously been reported by Ishihara[62-63] that catalyze Diels-Alder reactions through a double effect of intra

molecular hydrogen binding interactions and attractive π-π donor-acceptor interactions at their proposed transition state; however no further evidence for their model was provided. Furthermore, previous work on synthetic pockets for DA reactions was reported in 2006 by Fujita and coworkers.[64] They reported an aqueous molecular host led to unusual selectivity in Diels-Alder reactions, which was explained in terms of the product inhibiting the aromatic stacking interactions through which the planar reagents bound to the host.

This chapter will focus on cage-shaped borates 6B, 7B and 12B (Scheme 1), which allowed almost exclusive access to 2-aryl-substituted dihydropyrones. The main objective is to explain the selectivity of these catalysts towards aromatic substrates, and to quantify the role of NCIs in the rate-limiting TSs.

2.2.2 Computational Methods

All calculations were carried out using Gaussian09[50]. Transition state geometries were optimized using B97-D/TZV *(2d,2p)*.[40-42] Vibrational frequencies were calculated at the same levels of theory, and the SMD model[65] was used to account for the solvent effects (dichloromethane). Single point energy calculations at the M06-2X/TZV*(2d,2p)* level of theory were combined with B97-D free energy corrections to provide the final predicted free energies. Transitions states were located using the Berny Algorithm[46,47] and characterized by the existence of a single imaginary vibrational frequency (first order saddle point). For the uncatalyzed process a total of three aldehydes were studied: ethanal (2a), benzaldehyde (2b) and perfluorobenzaldehyde (2c). Three of the catalysts were evaluated: 6B, 7B and 12B.

2.2.3 Results and Discussion

2.2.3.1 Uncatalyzed Process

Before tackling the catalyzed HDA reactions, we first examined the mechanism of the uncatalyzed process for the cycloaddition of 2a-c with DD. For each reaction, there are two possible transition states: one where the substituents of the dienophile are oriented towards of the diene (endo) and the second one where they are oriented away (exo). Since a racemic mixture of the product is assumed based on the results reported by Baba and coworkers,[58] initially, both of those transition states were considered.

Computed barriers for the endo and exo HDA cycloaddition of 2a-c with DD are listed in Table 7. In every case, except for ethanal (2a), the endo TS was the lowest reaction pathway. IRCs were used to validate the TSs that were located; they were evaluated starting from the TS structure and confirm that the uncatalyzed process proceeds through this concerted by highly asymchronous process.

Table 7 Activation Energies for uncatalyzed HDA at the B97-D/TZV*(2d,2p)*//M06-2X/TZV*(2d,2p),* SMD level of theory

			Bond Distance [Å]	
Subs	**TS**	**$\Delta G^{\ddagger}$[kcal*mol^{-1}]**	C-C	C-O
2a	Endo	30.5	1.86	2.35
2a	Exo	30.0	1.86	2.41
2b	Endo	29.0	1.87	2.27
2b	Exo	30.0	1.85	2.31
2c	Endo	25.5	1.83	2.21
2c	Exo	24.5	1.88	2.4

2.2.3.2 Catalyzed Process

We next turn to the HDA cycloaddition of 2a and 2b catalyzed by 6B, 7B, and 12B (substrate 2c was not considered in this preliminary study). This reaction was found to be a two-step process. The overall mechanism of the catalyzed process is depicted in Figure 7. The reaction starts with the activation of the aldehyde (**Subs**) by the catalyst (**Cat**) to afford a Lewis adduct (**LA**). Upon addition of Danishefsky's diene (**DD**), initial C-C bond formation proceeds without a barrier to yield a zwitterionic intermediate (**ZInt**). Our data indicate that ZInt is the resting state of the catalytic cycle. The rate-limiting step is then the C-O bond formation (**TS2**), which provides the dihydropyrone precursor (**PDP**). It is feasible that this process would lead to either an endo or exo- product. However, only the endo path will be discussed here since it was found to be lower-lying. Upon acidic work up, **PDP** affords the desired product (**DP**). Computed free energies for each of the stationary points along this mechanism, relative to **Zint**, are listed in Table 8.

Table 8 Free Energies in kcal/mol relative to Zint @B97-D/TZV*(2d,2p)*//M06-2X/TZV*(2d,2p)*, SMD

Subs	Catalyst	Cat + Subs + DD	LA	Zint	$\Delta G^{\ddagger}$ (TS2)	PDP
2a	6B	7.6	5.2	0.0	9.7	-1.7
2b	6B	6.4	3	0.0	11.3	-2.0
2a	7B	9.4	5.4	0.0	8.7	-5.1
2b	7B	6.6	2.1	0.0	7.9	-0.9
2a	12B	10.7	6.4	0.0	9.5	-5.2
2b	12B	5.5	-0.8	0.0	9.3	-6.0

Figure 7 Catalytic Cycle for the HDA cycloaddition of 2a and 2b to DD catalyzed by 6B, 7B, and 12B

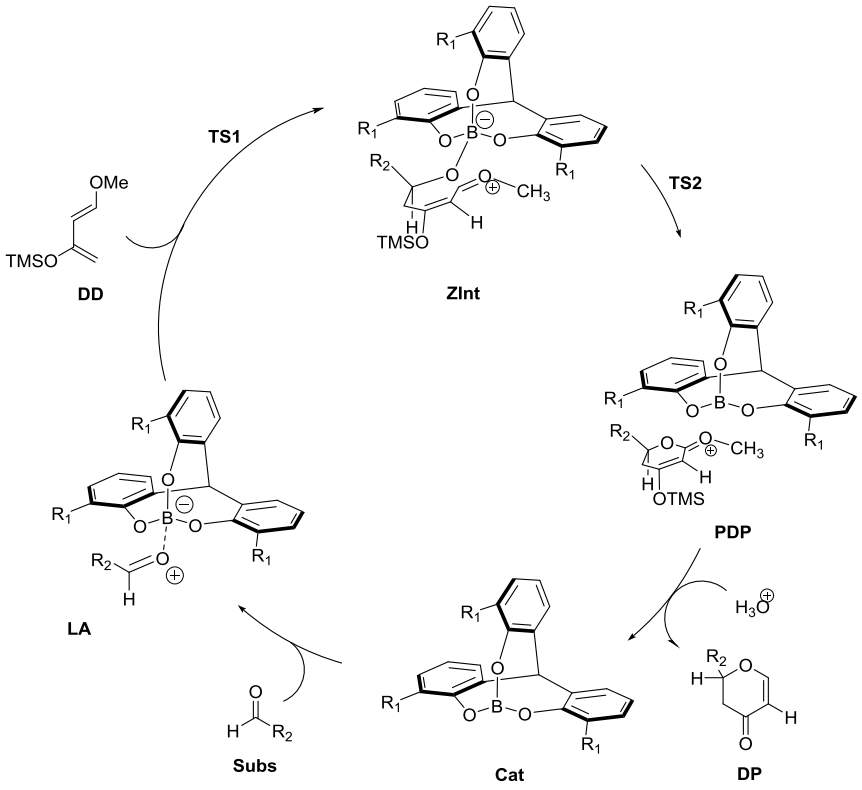

We predict low activation energies for both substrates and all three catalysts. However, our main concern here is the relative barriers for the aliphatic (2a) and aromatic (2b) substrates for each catalyst. We find that catalyst 6B, which lacks a "π-pocket," provides a lower activation energy for 2a compared to 2b. This is consistent with the observations of Baba and co-workers. However, for both 7B and 12B, which feature phenyl and naphthyl groups surrounding the reaction center, we correctly predict a greater reaction rate for 2b over 2a. Again, this is consistent with Baba's observations. However, the magnitude of the relative barriers is not fully consistent with Baba's rate data. In particular, Baba found that 12B provided greater selectivity for the aromatic aldheyde compared to 7B.

We are unable to reproduce this behavior, and predict only a slight preference for 2b over 2a when examining catalyst 12B.

With these results in hand, the non-covalent interactions between the reaction center and the π-pockets of catalyst 7B and 12B in **TS2** were analyzed more closely. The common, core structure, catalyst 6B, was removed. and the interaction energies between the aromatic rings and the TS structure were calculated. Results are shown in Table 9. For both catalysts, we find that there are more stabilizing interactions between the aromatic aldehyde (2b) and the p-pocket of the catalyst, compared to the aliphatic aldehyde. Although these data are in qualitative agreement with the proposed model of Baba and co-workers, the magnitude of this difference (0.3 to 0.4 kcal/mol) is not sufficient to explain the trend in barrier heights.

Table 9 Contribution of π pocket to chemoselectivity

Catalyst	Subs	Interaction with π-pocket [kcal/mol]
7B	**2a**	-3.8
7B	**2b**	-4.1
12B	**2a**	-6.3
12B	**2b**	-6.7

2.2.4 Summary and Conclusions

NCIs involved in the chemoselective HDA reaction reported by Baba and coworkers[58] were quantified. It was found that non-covalent interactions occurring with the π-pocket of catalysts 7B and 12B slightly favor the aromatic substrate (2b) over the aliphatic substrate (2a). The weak point in Baba's model stems from the fact that the rate of these reactions will be determined by the relative energy of **TS2** compared to the zwitterionic intermediate (**ZInt**). However, π-stacking interactions of the substrate with the p-pocket will occur in both of these structures, so should cancel to a large extent. As such, we think that the ultimate explanation of the chemoselectivity for aromatic aldehydes exhibited by 7B and 12B will not involve π-stacking interactions, but presumably arises from a combination of other factors. These will be pursued in future work, along with more thorough explorations of possible low-lying structures for **ZInt** and **TS2**.

3. TUNING NON-COVALENT INTERACTIONS INVOLVING CURVED POLYCYCLIC HYDROCARBONS THROUGH SUBSTITUENT EFFECTS

Dispersion interactions stem from the correlated motion of electrons in interacting molecules. More classically, these interactions can be understood as the induction of a dipole in one molecule caused by an instantaneous dipole in another molecule. Although dispersion interactions are a primary component of many types of NCIs, this chapter will mainly focus on two classes of dispersion-dominated interactions involving aromatic rings, depicted in Figure 8**Figure 8**, XH/π and π-stacking interactions. These interactions provide a potentially powerful means of controlling the assembly of curved polycyclic hydrocarbons, which are key components of novel organic electronic materials.

Figure 8 Prototypical π-stacking and XH/π interactions. The parallel-displaced configuration of the benzene dimer is 1 kcal/mol more strongly interacting than the sandwich dimer.

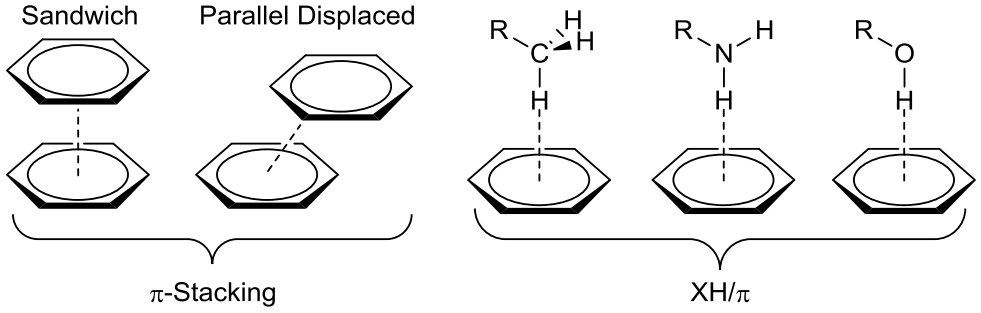

The effects of substituents on these aromatic interactions have been extensively studied both experimentally and computationally. Traditionally, substituent effects in π-stacking interactions were explained based on the pioneering models of Cozzi and Siegel[66-71]

and Hunter and Sanders.[72-75] In these models, substituent effects arise from the modulation of the π-electron density of the substituted aromatic system via resonance effects. In particular, electron-withdrawing groups enhance π-stacking interactions by depleting the π-electron density in the substituted ring, reducing the electrostatic repulsion between the π-clouds of the two rings. Electron-donating groups hinder π-stacking interactions through the opposite mechanism.

Despite the success of these venerable models in explaining stacking interactions in a myriad of systems, flaws in these models have emerged in recent years.[76-88] In particular, Wheeler and co-workers[83-88] have shown that substituent effects in π-stacking (and other non-covalent interactions involving aromatic rings)[85,87-91] are more rigorously described in terms of direct interactions between the substituents and the other ring. This built on earlier work from Wheeler and Houk[83] in which it was shown that substituent effects in the benzene sandwich dimer were retained even if the substituted phenyl ring was replaced with a hydrogen atom. Physically, these local, direct interactions can be understood as arising from the electrostatic interaction of the dipole moment associated with the substituent and C-H bond of the nearby vertex of the other ring.

The local nature of substituent effects in π-stacking interactions has important implications for substituent effects in stacking interactions of large, polycyclic aromatic systems. In particular, because substituent effects in the benzene dimer arise from the electrostatic interaction of the substituent with the nearby C-H bond, substituent effects will be qualitatively different in systems in which there is no C-H bond near the substituent. For example, Munusamy and Wheeler[92] recently showed that substituent effects in π-stacking interactions between substituted benzenes and carbon nanotubes (CNTs) are qualitatively

different than those in the benzene dimer. Moreover, substituent effects involving CNTs are driven by dispersion effects, not electrostatic effects as in the benzene dimer.

3.1 Background: Stacking of Curved Polyaromatic Hydrocarbons

Discotic polycyclic aromatic hydrocarbons have emerged as a key component for novel organic electronic materials. For example, discotic liquid crystals, which are organic materials that contain polycyclic aromatic hydrocarbons (PAHs) cores, were first reported by Chandrasekhar *et al*.[93] in 1977. They are characterized by their ability to self-assemble into columnar super-structures with high fluidity and excellent charge-carrier mobilities. These materials can be used as components of organic photovoltaics and nanoelectronics, as well as in molecular electronic applications in which high performance is gained by taking advantage of the intermolecular and mesoscopic ordering;[94] therefore, controlling the self-assembly of these materials is a key factor to improve their performance. Although significant progress has been made in recent years,[95] further improving the performance of these materials still remains a challenge.

Hexabenzocoronene (HBC, Figure 9a) is a popular discotic liquid crystal material, stemming largely from its high charge carrier mobility in such applications.[96-97] Strong π-stacking interactions between the large faces of these planar HBCs lead to well-ordered supramolecular aggregates, even in solution at low concentrations. Wheeler has shown,[98] computationally, that direct, local interactions between substituents and adjacent aromatic rings can provide a powerful means of controlling the local arrangements of model stacked discotic systems, including HBC.

Nuckolls and co-workers[99] recently synthesized a contorted isomer of hexabenzocoronene, c-HBC (Figure 9a). Steric interactions among the peripheral benzo rings of this system result in significant distortions from planarity, leading to a three-fold symmetric, doubly-concave geometry (see Figure 9b). The doubly-concave geometry of c-HBC portends intriguing possibilities for the assembly of mixed materials of c-HBC and fullerenes. In particular, contorted molecules such as c-HBC can self-stack, forming homodimers, or they can interact simultaneously with two C_{60} or C_{70}-fullerenes, one with each concave face of c-HBC. This opens the doors for the development of organic materials with well-ordered and alternating assemblies of c-HBC (as a donor) and C_{60} derivatives (such as PCBM, as an electron acceptor), for example (see Figure 9c). Indeed, Nuckolls and coworkers[100] have shown that *c*-HBC forms assembles with C_{70}, leading to functional bulk-heterojunction photovoltaic materials. The further development of such materials will require more refined control over the tendency of *c*-HBC to form either homodimers or heterodimers with fullerenes. That is, more refined materials will result from gaining control over the tendency for *c*-HBC/C_{60} mixtures to form alternating stacks or segregated assemblies of *c*-HBC and C_{60}.

Here, we use DFT methods to examine homodimers of substituted *c*-HBCs as well as complexes of substituted *c*-HBCs with C_{60}. The main goal is to quantify the effect of substituents on the binding energies of these non-covalent complexes and to explore whether substituent effects can be used to tune the propensity of *c*-HBC to form either homodimers or heterodimers with C_{60}.

Figure 9 (a) Hexabenzocoronene (HBC) and contorted-hexabenzocoronene (*c*-HBC); (b) two views of the B97-D/TZV*(2d,2p)* optimized structure of *c*-HBC, along with the geometric definitions of bowl-depth (BD) and bowl-radius (BR); (c) model of alternating C_{60}/*c*-HBC assembly.

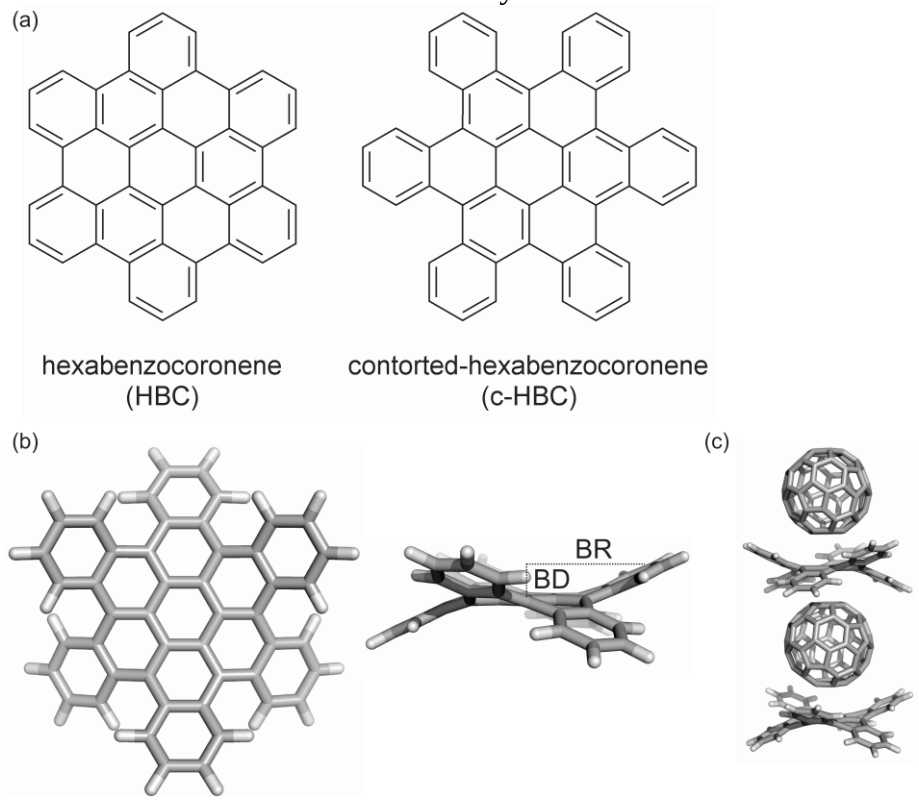

3.2 Theoretical Methods

We examined various model stacked complexes using DFT, all at the B97-D/TZV*(2d,2p)* level of theory. This dispersion-corrected functional, when paired with a triple-ζ basis set and density fitting techniques, provides accurate interaction energies and geometries for various π-stacked systems. All DFT computations were done using Gaussian 09 and employed density fitting techniques. SAPT0/jun-cc-pVDZ calculations were also carried out in select cases. SAPT0 computations were done using Psi4, and provide not only

total interaction energies, but also physical components of these interaction energies (electrostatic, exchange-repulsion, induction, and dispersion).

We were primarily concerned with substituted *c*-HBCs as shown below (Figure 10), in which the twelve peripheral hydrogens are replaced with one of SCH_3, NH_2, OCH_3, CH_3, CN, SH, C≡CH, OH, or F. These substituents span a broad range of donating and accepting character, and can be considered simple models of common alkyl and alkoxy solubilizing tails often attached to *c*-HBCs. We also considered perfluorinated *c*-HBC, *c*-HBC(F_{24}).

Figure 10 Substituted *c*-HBC

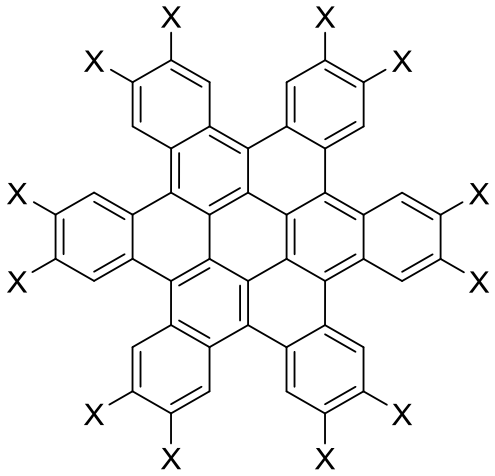

3.3 Results

3.3.1 Substituent Effects in Benzene-C_{60} Complexes

First, we studied model non-covalent interactions between monosubstituted benzenes and C_{60} (see Figure 11a), to understand the nature of substituent effects in π-stacking interactions involving the curved exterior of fullerenes. Interactions energies between 24 substituted benzenes and the hexagonal face of C_{60} are plotted against interaction energies for

the corresponding benzene sandwich dimers[86] in Figure 11b. Interaction energies in both the benzene-C_{60} and benzene-benzene dimers were computed by optimization the vertical separation of the two interacting rings while keeping the geometries of the molecules themselves fixed. These two stacked systems show drastically different substituent effects, despite the stacking interaction between outwardly similar hexagonal rings in both cases. This can be readily explained in terms of the local nature of substituent effects in π-stacking interactions.[86] In particular, the operative direct interactions in the C_{60}···benzene complexes are between the substituents and the "surface" of C_{60}. In general, these local, direct interactions between the substituent and C_{60}, which will consist of various XH/π interactions, will be qualitatively different from the direct interactions between the substituent and the C-H bonds of benzene that occur in the benzene sandwich dimer. As a result, substituent effects in stacking interactions between substituted phenyl rings and C_{60} can be tuned independently of those with other phenyl rings. Below, we will explore the possibility of using this ability to independently tune these different stacking interactions to control the tendency of substituted *c*-HBC to form either homodimers or complexes with C_{60}.

Figure 11 (a) Model complex of monosubstituted benzene over a hexagonal face of C_{60} and the monosubstituted benzene sandwich dimer; (b) Interaction energies (kcal/mol) of $C_6H_5X\cdots C_{60}$ versus $C_6H_6X\cdots C_6H_6$ sandwich dimers, relative to the unsubstituted cases, for a set of 24 substituents. Data for the benzene sandwich dimers are from ref [86].

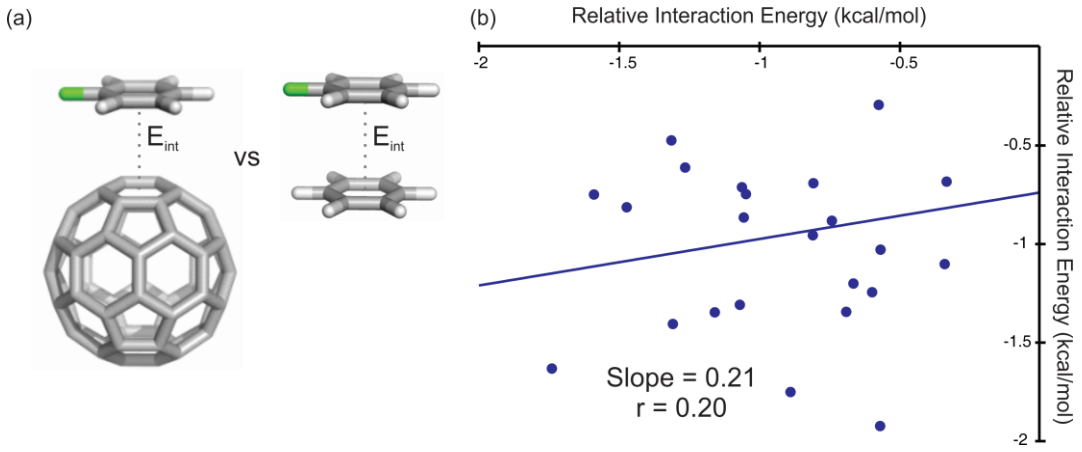

3.3.2 Unsubstituted c-HBC Homodimers and Complexes with C_{60}

Before delving into the effect of substituents on c-HBC homodimers and complexes of c-HBC with C_{60}, we first examine the corresponding unsubstituted complexes. Optimized structures of these two complexes are shown in Figure 12. Overall, the c-HBC$\cdots C_{60}$ complex shows a much shorter stacking distance (2.92 Å) compared to the c-HBC homodimer (3.59 Å). This arises because C_{60} can fit neatly inside the "cavity" of c-HBC, interacting strongly with both the coronene core of c-HBC and the appended benzo rings. The concavity of c-HBC changes significantly upon formation of complexes with either another c-HBC or C_{60}. In particular, in the homodimer, the depth of the concave bowl facing the other c-HBC is reduced to only 0.41 Å (compared to 0.96 Å in isolated c-HBC), whereas the depth of the "outer" bowl increases to 1.21 Å. The complex of c-HBC with C_{60} exhibits the opposite

behavior, with an increased bowl depth (to 1.26 Å) on the face of c-HBC complexed with C_{60} and a flattened bowl on the "outside" of the c-HBC.

Figure 12 B97-D optimized structures and binding energies (kcal/mol) of the c-HBC···c-HBC homodimer and c-HBC···C_{60} heterodimer.

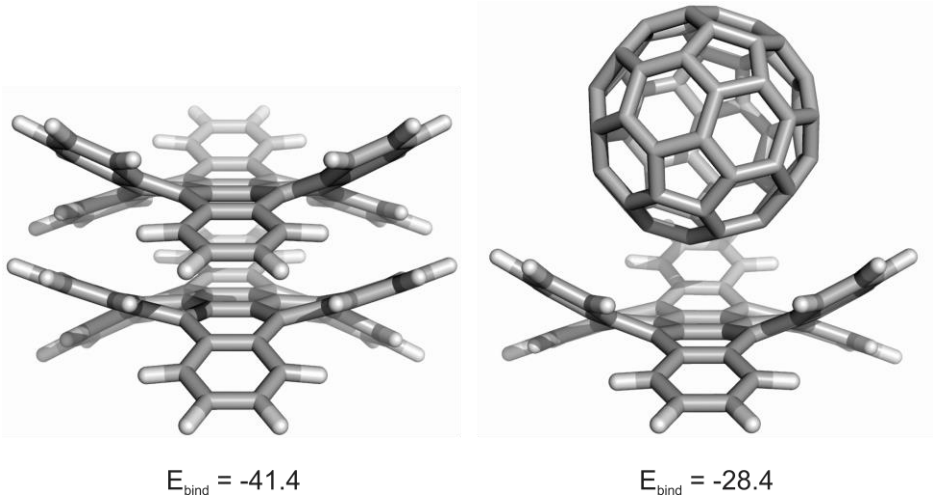

The predicted binding energies for c-HBC···c-HBC and c-HBC···C_{60} complexes are -41.4 and -28.4 kcal/mol, respectively. That is, both complexes are strongly bound in the gas phase, but, despite the shorter stacking distance in the c-HBC···C_{60} complex, the homodimer is more thermodynamically stable. However, the formation of mixed or segregated mixtures of C_{60} and c-HBC in the solid state does not just depend on the thermodynamics of formation of these dimers. The simplest possible model that differentiates between segregated and mixed aggregates of these two molecules is the conversion of c-HBC···c-HBC and C_{60}···C_{60} dimers to two c-HBC···C_{60} complexes. B97-D predicts the dissociation of the C_{60}···C_{60} dimer to require 8 kcal/mol. Based on this, the conversion of c-HBC···c-HBC + C_{60}···C_{60} into 2(c-HBC···C_{60}) is downhill by only 7.8 kcal/mol. However, in the solid state, aggregates of C_{60}

will go well beyond dimers, and breaking up these aggregates will cost more than the 8 kcal/mol required for the dimer. Thus, overall, for unsubstituted c-HBC, formation of mixed c-HBC/C_{60} assemblies is likely only slightly more thermodynamically favorable than formation of separate aggregates of C_{60} and c-HBC.

We next explore the dependence of the interaction energy on the orientation of C_{60} within the concave bonding pocket of c-HBC. Interaction energies for C_{60} with c-HBC as a function of rotations of C_{60} about the three Cartesian axes are shown in Figure 13. Although there are some variations (1 – 1.5 kcal/mol) in the interaction energy depending on the C_{60} orientation, these variations are small compared to the overall interaction energy (25 – 30 kcal/mol). Thus, even though we have attempted to locate the lowest-lying conformations in complexes of substituted c-HBC with C_{60} (see below), all of the conformers have similar interaction energies. Moreover, in the solid state, C_{60} is expected to exhibit nearly free rotation even if tightly packed within the concave pocket of c-HBC.

To further understand the dependence of the interaction energies in these dimers on the bowl depth of c-HBC, we examined model homo- and heterodimers involving c-HBCs with variable bowl depths ranging from the highly strained planar c-HBC to c-HBC with an artificially-deep concave pocket. We then computed interaction energies for stacked homodimers of these variably-curved c-HBCs their complexes with C_{60}. In these computations, we optimized the distance between the stacked systems, but did not alter the geometries of the molecules themselves.

Figure 13 Interaction energies (kcal/mol) of C_{60} with c-HBC as a function of rotations of C_{60} about the x, y, and z-axes.

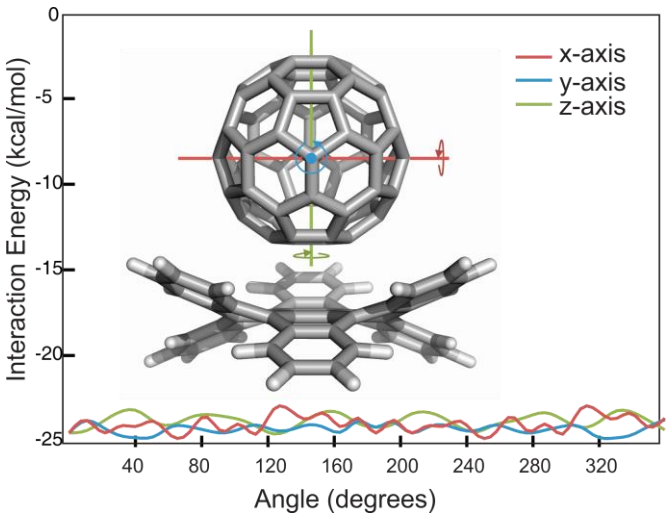

Interaction energies (relative to the constrained monomers) are plotted in Figure 14 for the homo- and heterodimers as a function of bowl depth. Also plotted is the strain energy of the c-HBC. First, we see that there is a steep energetic cost of distorting c-HBC away from the equilibrium bowl depth of 0.96 Å. For instance, the planar c-HBC lies nearly 160 kcal/mol higher in energy than the fully relaxed geometry.

More importantly, the data in Figure 14 reveal that the interaction energies for the homo- and heterodimers show very different dependence on the bowl depth of c-HBC. In particular, π-stacking interactions in c-HBC homodimers are maximized when the two c-HBCs have relatively shallow bowl depths. The homodimer with the most favorable interaction energy, having a bowl depth of 0.68 Å, is shown in Figure 15. The interaction energy here is more favorable than between purely planar c-HBCs because of the offset nature of the π-stacking interactions of the peripheral phenyl rings. That is, in the purely planar c-HBC homodimer, these phenyl rings are in a configuration resembling the benzene

sandwich dimer. Upon adopting a bowl depth of 0.68 Å, these same phenyl rings are now in a parallel displaced configuration, which, in the case of the benzene dimer, leads to a 1 kcal/mol stronger interaction. This is reflected in the ~10 kcal/mol greater interaction between two c-HBCs with bowl depths of 0.68 Å, compared to the homodimer of purely planar c-HBCs. Similar, for bowl depths exceeding 0.68 Å, favorable stacking interactions between the coronene cores and fused benzo rings of the two c-HBC give way to steric interactions and unfavorable edge-to-edge interactions. This is most prevalent in the dimer of the most contorted c-HBC examined, in which the bowl depth approaches 2 Å (Figure 14).

Figure 14 Strain energy (kcal/mol) of c-HBC as a function of bowl depth (dashed curve) as well as interaction energies (kcal/mol) for c-HBC homodimers (red curve) and c-HBC···C_{60} complexes (blue curve) as a function of bowl depth. The vertical, dotted line marks the bowl depth of the relaxed c-HBC monomer.

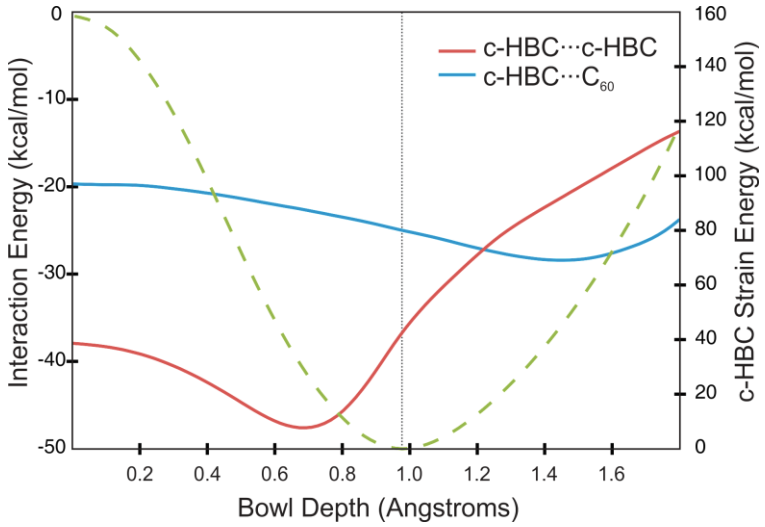

On the other hand, interaction energies in c-HBC···C_{60} complexes are maximized when the c-HBC adopts a more curved geometry, with a bowl depth of 1.46 Å. This is consistent with the observation that, in the optimized complex between c-HBC and C_{60}, there

was an increase in the bowl depth of the face of c-HBC bound to C_{60}. The corresponding structure is shown in Figure 15. In this case, the interaction energy is maximized because of optimal positioning of the peripheral benzo rings relative to the fullere, while still allowing C_{60} to engage in strong stacking interactions with the coronene core of c-HBC. As with the c-HBC homodimers, for c-HBC···C_{60} complexes, greater bowl depths lead to less favorable interaction energies because the geometry prevent close approach of the two molecules (see Figure 14).

Figure 15 c-HBC···c-HBC and c-HBC···C_{60} complexes with different bowl depths for the c-HBC.

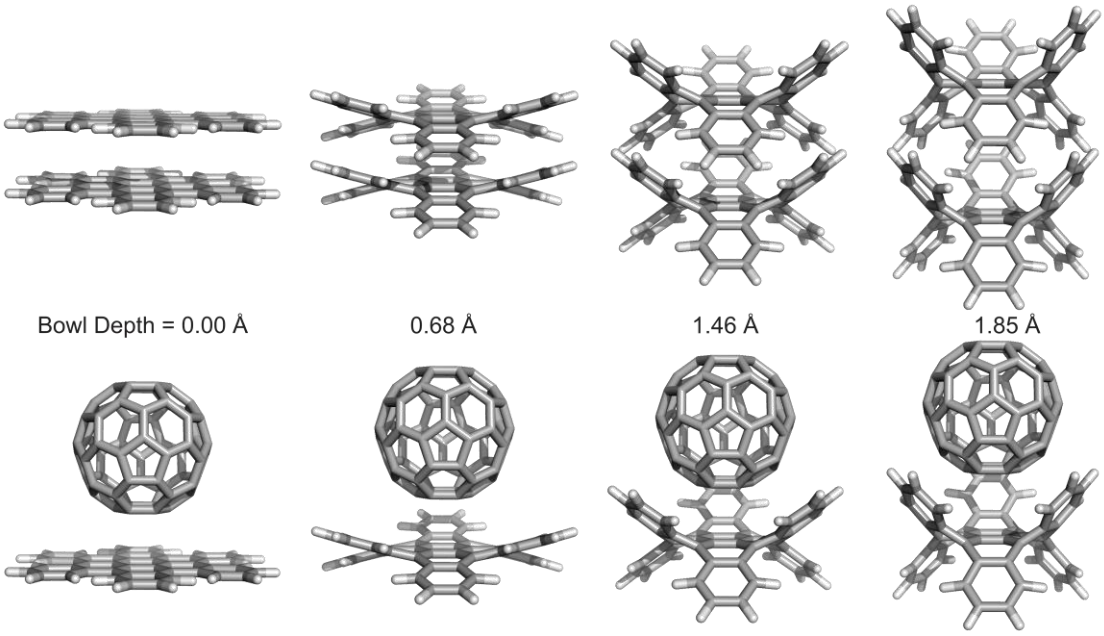

Overall, this data, combined with the observation that substituent effects with C_{60} are independent of those with other arenes, suggests two strategies for tuning the relative binding energies of c-HBC···C_{60} heterodimers and c-HBC homodimers. First, in the absence of other effects, if the bowl depth of c-HBC can be increased beyond the critical value of 1.25 Å (the

"crossover" point in the plot in (Figure 14), then such a system should exhibit greater affinity for C_{60} than itself. Alternatively, substituents that exhibit favorable direct interactions with C_{60}, but not with the phenyl rings of a stacked c-HBC, should also be able to stabilize the heterodimer but not the homodimer. Below, we explore the feasibility of using substituents to tune the non-covalent interactions in c-HBC homodimers and c-HBC$\cdots$$C_{60}$ complexes through both the direct interactions of substituents and the indirect impact of substituents on the curvature of c-HBCs.

3.3.3 Substituted c-HBC Monomers

First, however, we examine the impact of substituents on the geometries of c-HBC monomers. Table 10 shows computed bowl depths for c-HBCs substituted with 12 substituents around the periphery. Unfortunately, these substituents have minimal impact on the overall bowl geometry, providing only 0.07 Å of tunability. Based on the data in Figure 14, this will fall far short of the distortions required to tip the scales in favor of the c-HBC$\cdots$$C_{60}$ heterodimer solely based on the impact of bowl depth. Regardless, these substituted systems will allow us to assess the impact of direct substituent interactions on the relative stacking affinity of c-HBC with itself and with C_{60}. On the other hand, for perfluorinated c-HBC (see F_{24} entry in Table 10), there is a significant increase in the bowl depth to 1.34 Å, which exceeds the critical value of 1.25 Å required to preferentially form homodimers with C_{60}. This increased bowl depth can be attributed to steric interactions between the fluoro substituents. In this case, we will be able to probe the combined effects of direct substituent interactions and the substituent-induced changes in the bowl-depth of c-HBC.

Table 10 Bowl depths (in Å) for substituted c-HBC monomers, homodimers, and heterodimers with C_{60}. For the dimers, "inside" and "outside" refer to the faces of c-HBC facing towards or away from the other molecule, respectively.

		Heterodimer		Homodimer	
Substituent	**Monomer**	**Inside**	**Outside**	**Inside**	**Outside**
SCH_3	0.99	1.42	0.55	1.27	0.59
NH_2	0.92	1.40	0.51	0.85	0.87
OCH_3	0.93	1.40	0.56	1.14	0.62
CH_3	0.95	1.39	0.55	1.07	0.74
CN	0.99	1.53	0.48	1.03	0.94
SH	0.95	1.42	0.58	1.07	0.72
C≡CH	0.94	1.45	0.51	1.02	0.85
OH	0.93	1.28	0.65	1.00	0.76
H	0.96	1.32	0.60	1.15	0.68
F	0.96	1.42	0.58	1.08	0.73
F_{24}	1.34	1.59	0.87	1.26	1.02

3.3.4 Substituted c-HBC Homodimers and Complexes with C_{60}

Finally, we present binding energies (E_{bind}) for complexes of substituted *c*-HBCs both in homodimers and in heterodimers with C_{60} (See Table 11), along with the equilibrium separations (R_e). Surprisingly, for the *c*-HBC homodimers there is no correlation between R_e and E_{bind}. Most likely, the variations in the binding energies reflect the extent of interactions between substituents on the stacked *c*-HBCs, not so much the interaction with the core of *c*-HBC itself. On the other hand, for the *c*-HBC$^{\cdots}C_{60}$ heterodimers there is a modest inverse correlation ($r = -0.62$) between R_e and E_{bind}. That is, overall, the more strongly bound *c*-HBC$^{\cdots}C_{60}$ complexes correspond to those in which the C_{60} sits deeper in the concave binding pocket of *c*-HBC.

Figure 16 Optimized homodimers of $-NH_2$ and $-SCH_3$ substituted *c*-HBC, as well as homo- and heterodimer of *c*-HBC(F_{24}).

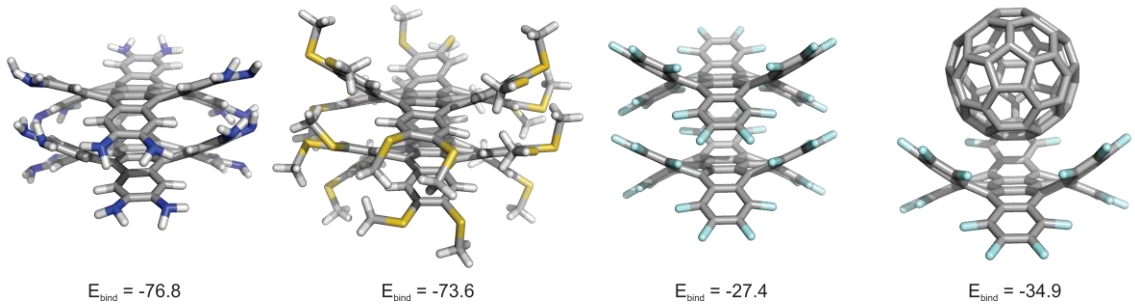

In the homodimers, all substituents result in significant enhancement of the binding energy, regardless of the nature of the substituent. This is reminiscent of substituent effects in the benzene dimer, for which all substituents lead to enhanced interaction (in the gas phase), compared to hydrogen, due to dispersion interactions between the substituent and the other ring.[76-79] Some of these substituent effects are substantial. For example, introduction of twelve NH_2 groups nearly doubles the binding energy compared to the unsubstituted dimer, and these substituents result in substantial deformations of the *c*-HBC (See Figure 16). In this case, the enhancement arises in part from the formation of intermolecular hydrogen bonds between the pendant amino groups. However, SCH_3 and OCH_3 also result in enhancements of the binding energy that are nearly as large, despite the obvious lack of hydrogen-bonding groups. In these cases, the enhanced binding is a likely a result of direct interactions between the substituents and the other *c*-HBC, and the *c*-HBC is once again significantly distorted. These direct substituent interactions are dominated by XH/π interactions with the highly polarizable phenyl rings of the stacked *c*-HBC.

Table 11 Binding energies (E_{bind}, kcal/mol) and distances (R_e, in Å) for homodimers of substituted *c*-HBCs as well as complexes of substituted *c*-HBCs with C_{60}.

	***c*-HBC···*c*-HBC Homodimers**		***c*-HBC···C_{60} Heterodimers**	
Substituent	R_e	E_{bind}	R_e	E_{bind}
SCH_3	3.45	-73.6	3.15	-38.4
NH_2	3.82	-76.8	3.68	-36.5
OCH_3	3.49	-68.7	3.42	-36.1
CH_3	3.63	-63.9	3.61	-33.5
CN	3.91	-45.5	3.29	-32.6
SH	3.63	-73.7	3.22	-31.7
C≡CH	3.79	-67.1	3.25	-31.3
OH	3.99	-64.4	3.2	-31.2
F	3.62	-51.2	2.92	-29.1
H	3.59	-41.4	2.92	-28.4
F_{24}	5.31	-27.4	3.24	-34.9

For heterodimers with C_{60}, the substituent effects are much more modest, yet result in enhanced interaction for all of the substituents. Once again, SCH_3, NH_2, and OCH_3 provide the greatest enhancement of the binding energy. Somewhat surprisingly, based on the lack of correlation between substituent effects in benzene···C_{60} dimers and the benzene sandwich dimer, there is a reasonable correlation (r = 0.84) between binding energies in the *c*-HBC···*c*-HBC and *c*-HBC···C_{60} complexes. Unfortunately, for all of the other substituents, the predicted binding energy for the *c*-HBC homodimer is always significantly more favorable than that of the *c*-HBC···C_{60} complex.

The only exception is the perfluoro *c*-HBC, F_{24}. In this case, the binding energy in the heterodimer (-34.9 kcal/mol) is significantly more favorable than the homodimer (E_{bind} = -27.4 kcal/mol). In this case, we predict that the heterodimer will clearly form preferentially over the homodimer, providing greater probability of formation of well-ordered alternating *c*-

HBC/C_{60} stacks. Presumably, this is a result of several factors. First, perfluorination of *c*-HBC pushes the bowl depth well beyond the critical value of 1.25 Å. This alone should lead to the heterodimer being about a 5 kcal/mol more strongly bound than the homodimer. Moreover, there are also unfavorable F···F interactions operative in the homodimer of *c*-HBC(F_{24}), which further tip the thermodynamic balance towards formation of the homodimer.

Table 12 SAPT0 total interaction energies as well as individual components of the SAPT0 interaction energies for substituted homodimers and heterodimers.

Substituent	SAPT0	Electrostatic	Exchange	Induction	Dispersion
Homodimers					
NH_2	-106.0	-64.1	121.5	-19.5	-144.0
OCH_3	-170.5	-47.3	106.3	-14.6	-151.4
CH_3	-89.2	-43.3	118.5	-12.9	-151.5
CN	-99.7	-35.2	92.0	-10.1	-146.4
SH	-89.4	-51.2	103.7	-15.9	-126.0
C≡CH	-81.3	-32.2	99.5	-10.4	-138.2
OH	-65.6	4.0	72.8	-18.3	-124.1
F	-61.2	-21.2	63.7	-6.1	-97.6
H	-61.6	-19.9	66.1	-7.4	-100.4
Heterodimers					
SCH_3	-66.9	-29.3	68.9	-6.8	-99.7
NH_2	-63.1	-32.2	70.2	-9.8	-91.2
OCH_3	-59.7	-27.3	63.4	-6.8	-89.0
CH_3	-61.2	-27.9	61.6	-7.7	-87.3
CN	-56.8	-21.0	50.9	-7.9	-78.9
SH	-59.0	-24.3	55.0	-5.4	-84.3
C≡CH	-57.8	-23.1	53.0	-5.2	-82.5
OH	-53.7	-25.3	56.2	-6.2	-78.3
F	-48.3	-21.4	49.5	-4.9	-71.4
H	-49.4	-21.3	47.7	-5.4	-70.3

Finally, in an attempt to understand the physical nature of the substituent effects in both the homodimers and complexes of *c*-HBC with C_{60}, we also performed SAPT0 computations on the substituted complexes. The total SAPT0 interaction energies, as well as the four components of these interaction energies (electrostatic, exchange-repulsion, induction, and dispersion) are included in Table 12. Unfortunately, these data suggest that none of these individual components is responsible for the observed trends in interaction energies. Moreover, we were unable to find any strong correlations between computed binding energies and Hammett constants or molar refractivity constants.

3.4 Summary and Conclusions

Substituent effects provide a potentially powerful means of tuning the non-covalent interactions between polycyclic systems, including curved systems such as *c*-HBC and fullerenes. We set out to explore the feasibility of using substituents to tune the relative stability of homodimers of *c*-HBC and *c*-HBC$^{\cdots}C_{60}$ complexes. For the unsubstituted case, the homodimers are more strongly bound.

Ultimately, we were able to show that full fluorination of *c*-HBC leads to preferential formation of *c*-HBC$^{\cdots}C_{60}$ complexes over *c*-HBC homodimers. However, for more modestly substituted systems, the *c*-HBC homodimers were still more strongly bound regardless of the nature of the substituents. This seems to stem from the relatively "flat" character of *c*-HBC, which is impacted little by substituents. Overall, substituent effects on *c*-HBC$^{\cdots}C_{60}$ complexes were modest compared to those in *c*-HBC homodimers, presumably because substituents on *c*-HBC are substantially farther away from the surface of C_{60} in the heterodimers than they are from the other *c*-HBC in the homodimers. Moreover, the

potential for intermolecular interactions between substituents in the case of the *c*-HBC homodimers is obviously not possible in complexes with C_{60}.

More generally, we showed that the simplest means of designing c-HBCs that preferentially bind C_{60} is to increase the bowl depth of the *c*-HBC. That is, we showed that the interaction of C_{60} with *c*-HBC is maximized when *c*-HBC adopts a bowl depth 1.46 Å; moreover, the *c*-HBC$^{\cdots}C_{60}$ heterodimer is more strongly bound than the *c*-HBC homodimer for bowl depths exceeding 1.25 Å. Achieving such a geometry with *c*-HBC requires an enormous amount of strain, which was only feasible through perfluorination. On the brighter side, complexes of C_{70} will require a shallower bowl depth, and the preferential of complexes of *c*-HBC with C_{70} over *c*-HBC homodimers will likely prove more feasible.

4. REVISITING THE ROTATIONAL BEHAVIOR OF PHENOLIC UNITS IN SUBSTITUTED PILLAR[5]ARENES

4.1 Background

Supramolecular chemistry continues to further the synthesis and study of innovative structures that could behave as hosts or guests with the final goal of observing new classes of interactions. Among the most relevant applications of these hosts is their ability to bind specific guests and even act as sensors for an assortment of analytes. Pillar[n]arenes, which are calixarane analogues first reported by Ogoshi *et al* in 2008,[101] serve as novel hosts for neutral and positively charged nitrogen compounds. Pillar[n]arenes are the product of the condensation of 1,4-dimethoxybenzene and formaldehyde in the presence of a Lewis acid; the [*n*] in the name indicates the number of hydroquinone units present in the macrocycle. In contrast to traditional calixaranes, which are bowl-shaped molecules, pillar[n]arenes exhibit relatively rigid, pillar-like architectures. This structural feature has contributed to the findings of Liu[102] and Zhang,[103] who have also reported the use of these pillar[5]arenes as monomers for linear supramolecular polymers. Pillar[*n*]arenes can also be used as components of roxatanes and are easier to functionalize than curcurbiturils.

The conformational behavior of pillar[5]arenes has been studied experimentally by Ogoshi and coworkers using variable temperature ^{1}H NMR.[101,104] The conformational behavior of these systems will play an important role in their role as guests in host-guest chemistry, and will also presumably impact the ability to incorporate pillar[n]arenes into linear supramolecular polymers and as components of rotaxanes. Intrigingly, Ogoshi and coworkers observed key differences in the rotational behavior between the –OH and–OMe

substituted pillar[5]arene. In particular, they found that the –OH substituted systems exhibited drastically slower conformational ring flips. This was attributed to intramolecular hydrogen bonds around the periphery of the pillar[n]arene. These H-bonds were not possible in the –OMe substituted system. Although Gejji and coworkers[105,106] previously studied these systems computationally, there has been no previous report of the effects of substituents the differences in conformational behavior. Below we describe a brief computational study aimed towards the understanding of the rotational behavior of –OH and –OMe substituted pillar[5]arenes.

Figure 17 Pillar[5]arenes: a) Synthesis; Crystal structure for b) - OH subsitituted pillar[5]arene and c) Crystal structure for -OMe substituted pillar[5] arene

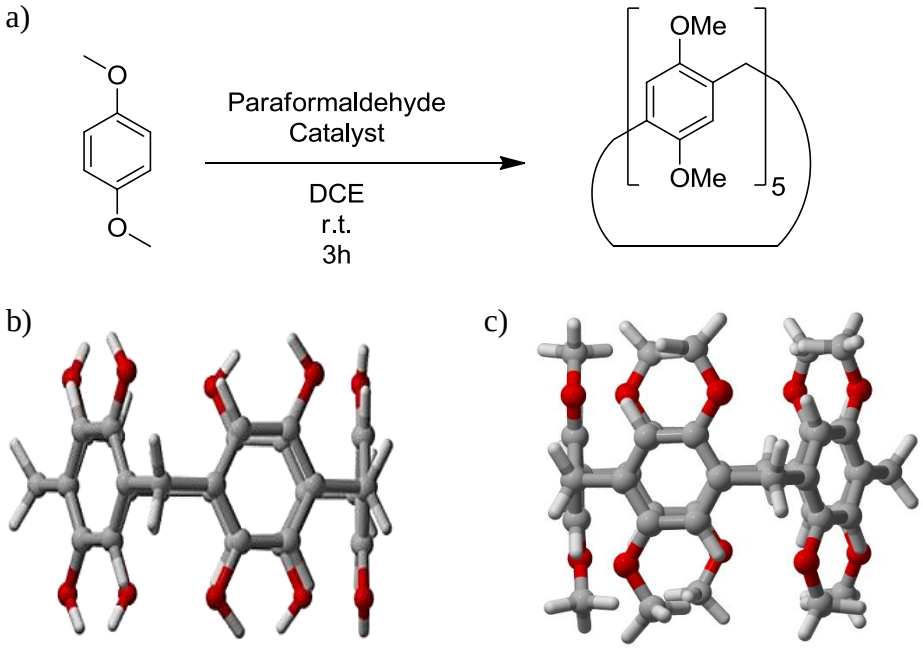

4.2 Computational Methods

Geometry optimizations were carried out using Gaussian 09.[50] Initially, torstional potential energy surfaces were obtained by performing a relaxed scan over specific dihedral angles. Starting from the energy minima and maxima found along this potential energy scan, when the located fully optimized minima and transition state geometries using B97-D/TZV*(2d,2p)*.[40-42] The PCM model[45,107] was used to account for solvent effects (acetone and methanol). Frequency calculations were performed at the same level of theory as those of the optimizations. Transitions states were located using the Berny Algorithm[46,47] and characterized by the existence of a single imaginary vibrational frequency (first order saddle points). To provide insight into the physical nature of substituent effects in these interactions, SAPT2/AVDZ energies were computed for fragments of the optimized B97-D/TZV*(2d,2p)* geometries. Single point energies were also calculated at the B97-D/TZV*(2d,2p)* level of theory for these truncated systems.

4.3 Results and Discussion

The Potential Energy surfaces (PESs) for the first ring flip of the –OH and –OMe substituted pillar[5]arenes were mapped out and referenced to the crystal structure conformation. Interesting observations can be made from these: first, the structure where the ring is completely flipped is a saddle point, not an energy minima. Most likely, in this configuration there is repulsion between the oxygens, causing the macrocycle to adopt a 'tilted' geometry. Second, considering only the rotation of a single ring, it is not obvious how hydrogen bonding would affect the rotational barrier of the –OH substituted pillar[5]arene.

Figure 18 a) Potential Energy Surface for first ring flip -OH and OMe substituted pillar[5]arenes in kcal/mol; b) TS1for -OH substituted (left) and -OME (right) pillar[5]arene; c) TS2 for -OH substituted (left) and -OME (right) pillar[5]arene

a)

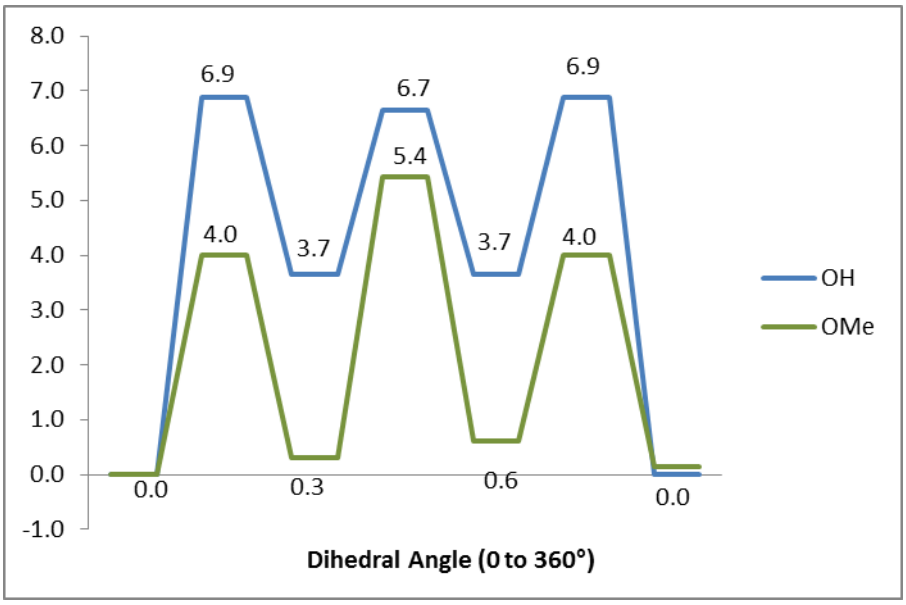

b)

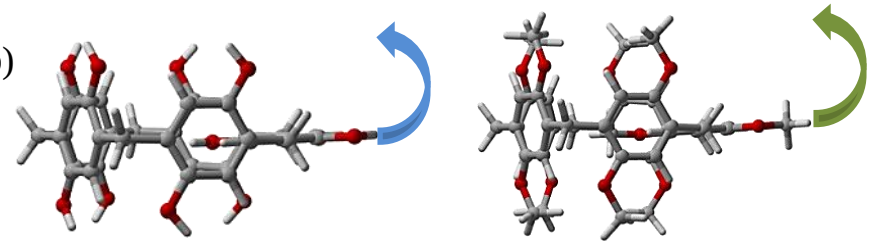

c)

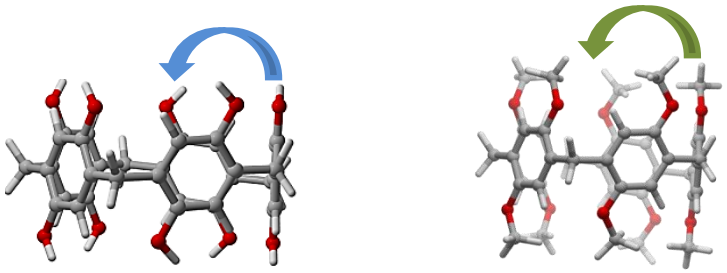

It was unexpected to observe that the TSs for both pillar[5]arenes were so similar, particularly considering that Ogoshi and coworkers explain the rotational speed difference in terms of hydrogen bond stabilization for the –OH case. At this point, our results would not immediately point in that direction. Moving forward in analyzing the rotational behavior of these materials an implicit solvent model was used to account for the observed discrepancy in rotational speed reported experimentally. It can be observed in Table 13 that for the –OH case, the inclusion of solvent effects drastically lowers the energy for all three TS structures. For the –OMe substituted case, on the other hand, it increases the first and third TS but lowers the second TS.

Table 13 Relative Energies in the gas-phase (GP), in acetone, and in methanol for the –OH and –OMe substitued pillar[5]arene structures.

	OH			OMe		
	GP	Acetone	Methanol	GP	Acetone	Methanol
Min1	0.0	0.0	0.0	0.0	0.0	0.0
TS1	6.9	-0.7	-0.7	4.0	0.4	0.5
Min2	3.7	-1.9	-1.9	0.3	0.2	0.3
TS2	6.7	-3.0	-3.2	5.4	-1.3	-1.4
Min3	3.7	-1.9	-1.9	0.6	0.0	0.1
TS3	6.9	-0.7	-0.7	4.0	0.4	0.5
Min4	0.0	0.0	0.0	0.1	-0.1	-0.1

With these results in hand, a step back was taken and other conformations for both the pillar[5]arenes were systematically evaluated for the first ring flip by only changing the orientation of the end group (-H or –OMe). It was found that for the –OH substituted case a lower conformation, favored by hydrogen bond, was possible. With this, the rotational barrier

for the –OH substituted pillar[5]arene is increased leading a slower speed of rotation supporting experimental observations . However, we were still intrigued by the energetic difference in the TSs given that both are almost identical (See Figure 19).

Figure 19 -OH substituted pillar[5]arene after one ring flip. The H-bond provides stabilization and helps slowing the rotation.

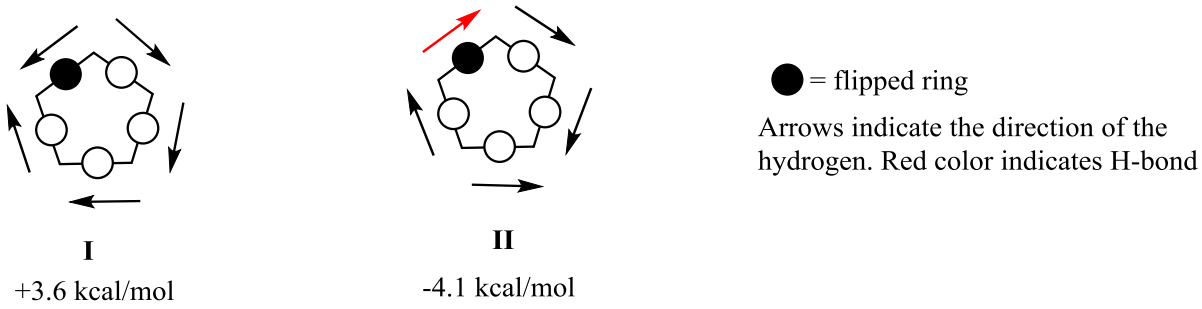

4.3.1 Dissecting the interactions: Understanding the components

The fully optimized structures for the TS leading to the first ring inversion as well as for both minima structures were then dissected into smaller model systems. In order to better understand the underlying origin of the interactions. We started by overlapping each of the structures for both, TSs and minima by doing this, we were able to pin-point those differences among the structures and to dissect them as shown into A, B and C. System A shows the flipping ring as it interacts with the left ring across the macrocycle and system B shows the interaction with the right ring across the macrocycle. These simplified systems reveal an that a significant factor to the difference in rotational speed between the –OH and –OMe substituted pillar[5]arene are CH-π interactions. These interactions are absent in the –OH substituted one case while they stabilize the –OMe TS by more than 1 kcal/mol each

leading to a lower barrier and a faster rotational speed. These results are qualitatively in line with SAPT calculations as shown in Table 14.

Figure 20 Overlapped transition states structures for single-ring flip of 1 (red) and 2 (blue), along with model systems (top = interaction @minimum non-flipped; bottom: Interaction @TS1- first ring flip).

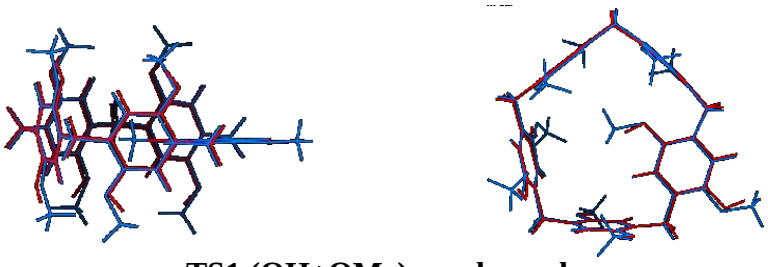

TS1 (OH+OMe) overlapped

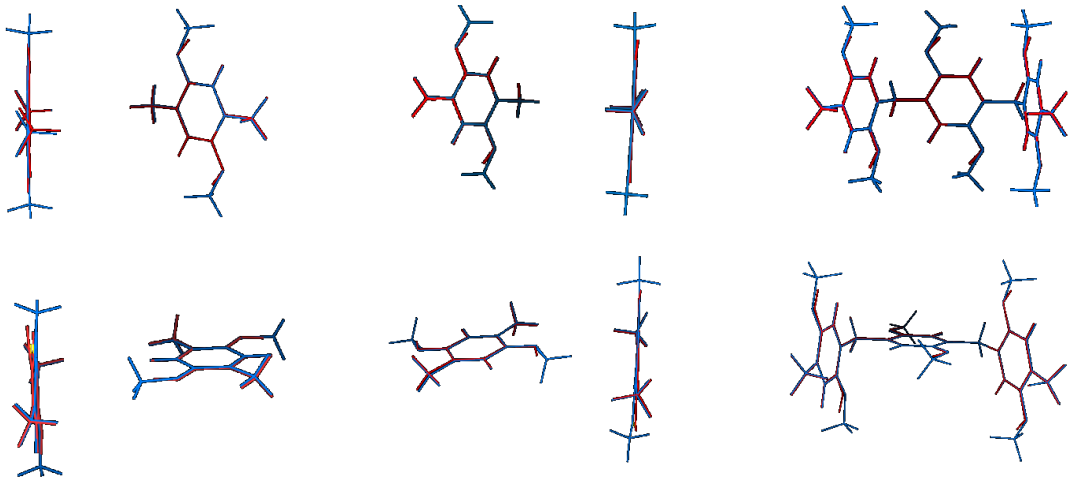

A **B** **C**

Table 14 SAPT interaction energies for model systems A and B of substituted pillar[5]arenes

Diff. Energy	A-OH	B-OH	A-OMe	B-OMe
Electrostatic	-0.45	-0.13	-0.69	-1.15
Exchange	0.01	0.02	0.34	1.23
Induction	-0.04	-0.04	-0.09	-0.27
Dispersion	-0.29	-0.36	-1.43	-2.13
SAPT2	-0.77	-0.50	-1.87	-2.32

In order to better support our hypothesis that CH/ π interactions are for the difference in the rotational behavior of these substituted pillar[5]arenes, we decided to calculate their energetic differences using a DFT method that would not capture dispersion. By doing so, one would expect the barrier to be diminished. The results at the B3LYP/6-31+g* level of theory are shown below and as expected, the energetic gap is smaller due to the failure of the method of capturing the stabilizing CH/π interactions at TS1 as shown below in Table 15.

Table 15 TS barriers calculated at the B97-D/TZV*(2d,2p)* and B3LYP/6-31G+(d) levels of theory

TS1 vs. ground state	B97D/TZV(2d.2p)	B3LYP/6-31+G(d)
-OH Pillar[5]arene	6.8 kcal/mol	8.9 kcal/mol
-OMe Pillar[5]arene	3.8 kcal/mol	7.8 kcal/mol

4.4 Summary and Conclusions

In conclusion, we have presented a computational study of the rotational behavior of substituted pillar[5]arenes at the DFT and SAPT2 levels. The results offer a more complete explanation for the difference in rotational speed for these substituted pillar[5]arenes. First, the results agree with the hydrogen bond stabilization explanation provided by Ogishi[108] and coworkers[108] for the –OH substituted case. Second, the data clearly show that the CH/π interactions stabilize the TS structures and lower the rotational barriers of the OMe-substitued systems. Ultimately, this work suggests an alternative, previously unexplored means of tuning the conformational behavior of pillar[*n*]arenes. In particular, it points out the potential to facilitate rotation of the phenolic units through stabilizing intramolecular non-covalent XH/π interactions in the TS structures. In this context, pillar[5]arenes provide a potentially powerful platform to experimentally probe the impact of solvent and aryl substituents on the strength of XH/ π interactions. Such probes have proved invaluable in studies aimed at unraveling the origin of substituent effects in sundry non-covalent interactions.

5. SUMMARY

Density functional theory and ab initio methods have been used to study the contribution of NCIs to organocatalyzed processes and two novel organic materials. It was shown that modern DFT methods have become a valuable tool for organic chemists in studies of systems in which dispersion-driven NCIs are vital. Such applications of DFT would not have been possible a decade ago.

Allylation and propargylation reactions catalyzed by Nakajima's bipyridine *N*,*N*'-dioxide catalyst were used as an example to benchmark DFT methods against high accuracy *ab initio* calculations. It was shown that B97-D/TZV*(2d,2p)* provides the best compromise of accuracy for individual TS structures and overall predictions of stereoselectivies for these reactions. Furthermore, we showed that the stereoselectivity of Nakajima's bipyridine *N*,*N*'-dioxide catalysts arises from electrostatic interactions with the chiral environment of the hexacoordinate silicon. Indeed, Nakajima's original TS model was based on the wrong arrangement of ligands around this hexacoordinate silicon. Overall, this work lays the foundation for the future use of this functional in the screening and rational design of bipyridine *N*,*N*'-dioxides for asymmetric propargylations.

A HDA reaction catalyzed by cage-shaped borate catalysts designed by Baba and coworkers was studied at the M06-2X/TZV*(2d,2p)* level of theory. Although not definite, the results provide some support that π-stacking interactions with the catalyst are responsible for the selective reaction of aromatic over aliphatic aldehydes, as observed experimentally.

In an effort to better control the properties of discotic liquids, stacking interactions between *c*-HBC homodimers and *c*-HBC $-C_{60}$ heterodimers were studied using B97-D/TZV*(2d,2p)* level of theory. It was found that, by controlling the curvature of the *c*-HBC,

the preference to stack as homo or heterodimers can be tuned. To achieve this, different substituents on the *c*-HBC were tested and only the perfluorinated (F_{24}) case was observed to steer the preference towards the *c*-HBC – C_{60} heterodimer. These results provide a guide to experimental chemists by saving time to synthesize and screen only the promising substituents.

Finally, an additional explanation was provided for the rotational speed difference between the –OH and –OMe substituted pillar[5]arenes. A computational study using B97-D/TZV*(2d,2p)* showed that in addition to the hydrogen bond explanation for the –OH substituted case provided by Ogishi and coworkers, CH/π interactions contribute significantly to the TS stabilization of the –OMe substituted case and therefore lowering the rotational speed.

REFERENCES

(1) Knowles, R. R.; Jacobsen, E. N. *P Natl. Acad. Sci. USA* **2010**, *107*, 20678-20685.

(2) Wheeler, S. E.; Bloom, J. W. G. *J. Phys. Chem. A* **2014**,*118*, 6133.

(3) Čížek, J. *J. Chem. Phys.* **1966**, *45*, 4256-4266.

(4) Čižek, J.; Paldus, J. *Int. J. Quant. Chem.* **1971**, *5*, 359-379.

(5) Paldus, J.; Čížek, J.; Shavitt, I. *Phys. Rev. A* **1972**, *5*, 50-67.

(6) Purvis, G. D.; Bartlett, R. J. *J. Chem. Phys.* **1982**, *76*, 1910-1918.

(7) Neese, F.; Wennmohs, F.; Hansen, A. *J. Chem. Phys.* **2009**, *130*, 114108.

(8) Neese, F.; Wennmohs, F.; Hansen, A.; Grimme, S. *Acc. Chem. Res.* **2009**, *42*, 641-648.

(9) Kollmar, C.; Neese, F. *Mol. Phys.* **2010**, *108*, 2449-2458.

(10) Bachrach, S. M.; John Wiley & Sons, Inc: 2007.

(11) Burke, K., *J. Chem. Phys.* **2012**, *136*, 150901.

(12) Bahmanyar, S.; Houk, K. N. *J. Am. Chem. Soc.* **2001**, *123*, 12911-12912.

(13) Bahmanyar, S.; Houk, K. N. *J. Am. Chem. Soc.* **2001**, *123*, 11273-11283.

(14) Allemann, C.; Gordillo, R.; Clemente, F. R.; Cheong, P. H. Y.; Houk, K. N. *Accounts Chem Res* **2004**, *37*, 558-569.

(15) Clemente, F. R.; Houk, K. N. *Angew. Chem. Int. Edit.* **2004**, *43*, 5766-5768.

(16) Shinisha, C. B.; Sunoj, R. B. *Org. Biomol. Chem.* **2008**, *6*, 3921-3929.

(17) Cheong, P. H. Y.; Legault, C. Y.; Um, J. M.; Celebi-Olcum, N.; Houk, K. N. *Chem. Rev.* **2011**, *111*, 5042-5137.

(18) Dieckmann, A.; Beniken, S.; Lorenz, C. D.; Doltsinis, N. L.; von Kiedrowski, G. *Chem-Eur J* **2011**, *17*, 468-480

(19) Nakajima, M.; Saito, M.; Hashimoto, S. *Tetrahedron: Asymmetry***2002**, *13*, 2449-2452.

(20) Nakajima, M.; Saito, M.; Hashimoto, S. *Chem. Pharm. Bull.* **2000**, *48*, 306-307.

(21) Nakajima, M.; Saito, M.; Shiro, M.; Hashimoto, S. *J. Am. Chem. Soc.* **1998**, *120*, 6419-6420.

(22) Lu, T. X.; Zhu, R. X.; An, Y.; Wheeler, S. E. *J. Am. Chem. Soc.* **2012**, *134*, 3095-3102.

(23) Lu, T.; Porterfield, M. A.; Wheeler, S. E. *Org Lett* **2012**.

(24) Haruta, R.; Ishiguro, M.; Ikeda, N.; Yamamoto, H. *J. Am. Chem. Soc.* **1982**, *104*, 7667-7669.

(25) Ikeda, N.; Arai, I.; Yamamoto, H. *J. Am. Chem. Soc.* **1986**, *108*, 483-486.

(26) Malkov, A. V.; Ramirez-Lopez, P.; Biedermannova, L.; Rulisek, L.; Dufková, L.; Kotora, M.; Zhu, F.; Kočovky, P. *J. Am. Chem. Soc.* **2008**, *130*, 5341-5348.

(27) Hrdina, R.; Opekar, F.; Roithová, J.; Kotora, M. *Chem. Commun.* **2009**, 2314-2316.

(28) Hrdina, R.; Opekar, F.; Roithova, J.; Kotora, M. *Chem. Commun.* **2009**, 2314-2316.

(29) Denmark, S. E.; Coe, D. M.; Pratt, N. E.; Griedel, B. D. *J. Org. Chem.* **1994**, *59*, 6161-6163.

(30) Denmark, S. E.; Fu, J. P. *J. Am. Chem. Soc.* **2000**, *122*, 12021-12022.

(31) Denmark, S. E.; Wynn, T. *J. Am. Chem. Soc.* **2001**, *123*, 6199-6200.

(32) Denmark, S. E.; Fu, J. P. *J. Am. Chem. Soc.* **2001**, *123*, 9488-9489.

(33) Denmark, S. E.; Beutner, G. L. *Angew. Chem. Int. Edit.* **2008**, *47*, 1560-1638.

(34) Denmark, S. E.; Fu, J. P. *Chem. Commun.* **2003**, 167-170.

(35) Becke, A. D. *J. Chem. Phys.* **1993**, *98*, 1372-1377.

(36) Lee, C. T.; Yang, W. T.; Parr, R. G. *Phys. Rev. B* **1988**, *37*, 785-789.

(37) Zhao, Y.; Truhlar, D. G. *Accounts Chem. Res.* **2008**, *41*, 157-167.

(38) Wodrich, M. D.; Corminboeuf, C.; Schleyer, P. V. *Org. Lett.* **2006**, *8*, 3631-3634.

(39) Zhao, Y.; Truhlar, D. G. *Theor. Chem. Acc.* **2008**, *120*, 215-241.

(40) Grimme, S. *J. Comput. Chem.* **2006**, *27*, 1787-1799.

(41) Grimme, S. *Wires Comput. Mol. Sci.* **2011**, *1*, 211-228.

(42) Goerigk, L.; Grimme, S. *Phys. Chem. Chem. Phys.* **2011**, *13*, 6670-6688.

(43) Schenker, S.; Schneider, C.; Tsogoeva, S. B.; Clark, T. *J. Chem. Theory Comput.* **2011**, *7*, 3586-3595.

(44) Tomasi, J.; Mennucci, B.; Cammi, R. *Chem. Rev.* **2005**, *105*, 2999-3093.

(45) Miertus, S.; Scrocco, E.; Tomasi, J. *Chem. Phys.* **1981**, *55*, 117-129.

(46) Peng, C. Y.; Ayala, P. Y.; Schlegel, H. B.; Frisch, M. J. *J. Comput. Chem.* **1996**, *17*, 49-56,

(47) Schlegel, H. B. *Theor. Chim. Acta* **1984**, *66*, 333-340.

(48) Weigend, F.; Ahlrichs, R. *Phys. Chem. Chem. Phys.* **2005**, *7*, 3297-3305.

(49) Kubas, A.; Braese, S.; Fink, K. *Chem: Eur. J.* **2012**, *18*, 8377-8385, S8377/1-S8377/18.

(50) Frisch, M. J., et al.; Revision B.01 ed.; Gaussian, Inc.: Wallingford CT,, 2009.

(51) MOLPRO, version 2010.1, is a package of ab initio programs written by H.-J. Werner, et al.

(52) Neese, F. *WIREs Comp. Mol. Sci.* **2012**, *2*, 73-78.

(53) Musher, J. I. *Angew. Chem. Chem. Int. Ed. Engl.* **1969**, *8*, 54-68.

(54) Tandura, S. N.; Voronkov, M. G.; Alekseev, N. V. *Top. Curr. Chem.* **1986**, *131*, 99-189.

(55) Takenaka, N.; Chen, J. S.; Captain, B. *Org. Lett.* **2011**, *13*, 1654-1657.

(56) Malkov, A. V.; Orsini, M.; Pernazza, D.; Muir, K. W.; Langer, V.; Meghani, P.; Kočovsky, P. *Org. Lett.* **2002**, *4*, 1047-1049.

(57) Hoffmann, R. W.; Landmann, B. *Chem. Ber.* **1986**, *119*, 1039-1053.

(58) Nakajima, H.; Yasuda, M.; Takeda, R.; Baba, A. *Angew. Chem. Int. Edit.* **2012**, *51*, 3867-3870.

(59) Yasuda, M.; Yoshioka, S.; Yamasaki, S.; Somyo, T.; Chiba, K.; Baba, A. *Org. Lett.* **2006**, *8*, 761-764.

(60) Yasuda, M.; Nakajima, H.; Takeda, R.; Yoshioka, S.; Yamasaki, S.; Chiba, K.; Baba, A. *Chem-Eur J* **2011**, *17*, 3856-3867.

(61) Guin, J.; Rabalakos, C.; List, B. *Angew. Chem. Int. Edit.* **2012**, n/a-n/a.

(62) Hatano, M.; Mizuno, T.; Izumiseki, A.; Usami, R.; Asai, T.; Akakura, M.; Ishihara, K. *Angew. Chem. Int. Edit* **2011**, *50*, 12189-12192.

(63) Ishihara, K.; Kurihara, H.; Matsumoto, M.; Yamamoto, H. *J. Am. Chem. Soc.* **1998**, *120*, 6920-6930.

(64) Yoshizawa, M.; Tamura, M.; Fujita, M. *Science* **2006**, *312*, 251-254.

(65) Marenich, A. V.; Cramer, C. J.; Truhlar, D. G. *J. Phys. Chem. B* **2009**, *113*, 6378-6396.

(66) Cozzi, F.; Cinquini, M.; Annunziata, R.; Dwyer, T.; Siegel, J. S. *J. Am. Chem. Soc.* **1992**, *114*, 5729-5733.

(67) Cozzi, F.; Cinquini, M.; Annunziata, R.; Siegel, J. S. *J. Am. Chem. Soc.* **1993**, *115*, 5330-5331.

(68) Cozzi, F.; Ponzini, F.; Annunziata, R.; Cinquini, M.; Siegel, J. S. *Angew. Chem. Int. Ed.* **1995**, *34*, 1019-1020.

(69) Cozzi, F.; Siegel, J. S. *Pure Appl. Chem.* **1995**, *67*, 683-689.

(70) Cozzi, F.; Annunziata, R.; Benaglia, M.; Cinquini, M.; Raimondi, L.; Baldridge, K. K.; Siegel, J. S. *Org. Biomol. Chem.* **2003**, *1*, 157-162.

(71) Cozzi, F.; Annunziata, R.; Benaglia, M.; Baldridge, K. K.; Aguirre, G.; Estrada, J.; Sritana-Anant, Y.; Siegel, J. S. *Phys. Chem. Chem. Phys.* **2008**, *10*, 2686-2694.

(72) Hunter, C. A.; Sanders, J. K. M. *J. Am. Chem. Soc.* **1990**, *112*, 5525-5534.

(73) Hunter, C. A.; Lawson, K. R.; Perkins, J.; Urch, C. J. *J. Chem. Soc., Perkin Trans. 2* **2001**, 651-669.

(74) Cockroft, S. L.; Hunter, C. A.; Lawson, K. R.; Perkins, J.; Urch, C., J. *J. Am. Chem. Soc.* **2005**, *127*, 8594-8595.

(75) Cockroft, S. L.; Perkins, J.; Zonta, C.; Adams, H.; Spey, S. E.; Low, C. M. R.; Vinter, J. G.; Lawson, K. R.; Urch, C. J.; Hunter, C. A. *Org. Biomol. Chem.* **2007**, *5*, 1062-1080.

(76) Sinnokrot, M. O.; Sherrill, C. D. *J. Phys. Chem. A* **2003**, *107*, 8377-8379.

(77) Sinnokrot, M. O.; Sherrill, C. D. *J. Am. Chem. Soc.* **2004**, *126*, 7690-7697.

(78) Ringer, A. L.; Sinnokrot, M. O.; Lively, R. P.; Sherrill, C. D. *Chem. Eur. J.* **2006**, *12*, 3821-3828.

(79) Sinnokrot, M. O.; Sherrill, C. D. *J. Phys. Chem. A* **2006**, *110*, 10656-10668.

(80) Arnstein, S. A.; Sherrill, C. D. *Phys. Chem. Chem. Phys.* **2008**, *10*, 2646-2655.

(81) Hohenstein, E. G.; Duan, J.; Sherrill, C. D. *J. Am. Chem. Soc.* **2011**, *133*, 13244-13247.

(82) Watt, M.; Hardebeck, L. K. E.; Kirkpatrick, C. C.; Lewis, M. *J. Am. Chem. Soc.* **2011**, *133*, 3854-3862.

(83) Wheeler, S. E.; Houk, K. N. *J. Am. Chem. Soc.* **2008**, *130*, 10854-10855.

(84) Wheeler, S. E.; McNeil, A. J.; Müller, P.; Swager, T. M.; Houk, K. N. *J. Am. Chem. Soc.* **2010**, *132*, 3304-3311.

(85) Raju, R. K.; Bloom, J. W. G.; An, Y.; Wheeler, S. E. *Chem. Phys. Chem.* **2011**, *12*, 3116-3130.

(86) Wheeler, S. E. *J. Am. Chem. Soc.* **2011**, *133*, 10262-10274.

(87) Wheeler, S. E. *Acc. Chem. Res.* **2013**, *46*, 1029-1038.

(88) Wheeler, S. E.; Bloom, J. W. G. *J. Phys. Chem. A* **2014**, Article ASAP, DOI:10.1021/jp504415p.

(89) Wheeler, S. E.; Houk, K. N. *J. Am. Chem. Soc.* **2009**, *131*, 3126-3127.

(90) Wheeler, S. E.; Houk, K. N. *J. Chem. Theory Comput.* **2009**, *5*, 2301-2312.

(91) Wheeler, S. E.; Houk, K. N. *J. Phys.Chem. A* **2010**, *114*, 8658-8664.

(92) Munusamy, E.; Wheeler, S. E. *J. Chem. Phys.* **2013**, *139*, 94703.

(93) Sadashiva, B. K.; Suresh, K. A. *Pramana - J Phys* **1977**, *9*, 471-480.

(94) Schmidt-Mende, L.; Fechtenkötter, A.; Müllen, K.; Moons, E.; Friend, R. H.; MacKenzie, J. D. *Science (New York, N.Y.)* **2001**, *293*, 1119-1122.

(95) Pisula, W.; Feng, X.; Müllen, K. *Adv. Mat*. *22*, 3634-3649.

(96) Craats, A. M. v. d.; Warman, J. M.; Fechtenkötter, A.; Brand, J. D.; Harbison, M. A.; Müllen, K. *Adv. Mat.* **1999**, *11*, 1469-1472.

(97) Käfer, D.; Bashir, A.; Dou, X.; Witte, G.; Müllen, K.; Wöll, C. *Adv. Mat.* **2010**, *22*, 384-388.

(98) Wheeler, S. E. *Cryst. Eng. Comm.* **2012**, *14*, 6140-6145.

(99) Plunkett, K. N.; Godula, K.; Nuckolls, C.; Tremblay, N.; Whalley, A. C.; Xiao, S. *Org. Lett*. **2009**, *11*, 2225-2228.

(100) Kang, S. J.; Ahn, S.; Kim, J. B.; Schenck, C.; Hiszpanski, A. M.; Oh, S.; Schiros, T.; Loo, Y.-L.; Nuckolls, C. *J. Am. Chem. Soc.* **2013**, *135*, 2207-2212.

(101) Ogoshi, T.; Kanai, S.; Fujinami, S.; Yamagishi, T. A.; Nakamoto, Y. *J. Am. Chem. Soc.* **2008**, *130*, 5022-5023.

(102) Liu, L. Z.; Wang, L. Y.; Liu, C. C.; Fu, Z. Y.; Meier, H.; Cao, D. R. *J. Org. Chem.* **2012**, *77*, 9413-9417.

(103) Zhang, Z. B.; Luo, Y.; Chen, J. Z.; Dong, S. Y.; Yu, Y. H.; Ma, Z.; Huang, F. H. *Angew. Chem. Int. Edit.* **2011**, *50*, 1397-1401.

(104) Ogoshi, T.; Kitajima, K.; Aoki, T.; Yamagishi, T.; Nakamoto, Y. *J Phys. Chem. Lett*. **2010**, *1*, 817-821.

(105) Peerannawar, S. R.; Gejji, S. P. *Comput. Theor. Chem.* **2012**, *999*, 169-178.

(106) Peerannawar, S. R.; Gejji, S. P. *Phys. Chem. Chem. Phys.* **2012**, *14*, 8711-8722.

(107) Tomasi, J.; Mennucci, B.; Cammi, R. *Chem. Rev.* **2005**, *105*, 2999-3093.

(108) Ogoshi, T.; Kitajima, K.; Aoki, T.; Yamagishi, T.-a.; Nakamoto, Y. *J. Chem. Phys. Lett*, *1*, 817-821.